Volcanic Contribution to Decadal Changes in Tropospheric Temperature

Benjamin D. Santer[1], Céline Bonfils[1], Jeffrey F. Painter[1], Mark D. Zelinka[1], Carl Mears[2], Susan Solomon[3], Gavin A. Schmidt[4], John C. Fyfe[5], Jason N.S. Cole[5], Larissa Nazarenko[4], Karl E. Taylor[1] & Frank J. Wentz[2]

[1]Program for Climate Model Diagnosis and Intercomparison (PCMDI), Lawrence Livermore National Laboratory, Livermore, CA 94550, USA. [2] Remote Sensing Systems, Santa Rosa, CA 95401, USA. [3] Massachusetts Institute of Technology, Earth, Atmospheric, and Planetary Sciences, Cambridge, MA 02139, USA. [4]NASA/Goddard Institute for Space Studies, New York, NY 10025, USA. [5]Canadian Centre for Climate Modelling and Analysis, Environment Canada, Victoria, British Columbia, V8W 2Y2, Canada.

Submitted to *Nature Geoscience*: November 29, 2013

Revised: January 22, 2014

Despite continued growth in atmospheric levels of greenhouse gases, global-mean surface and tropospheric temperatures show slower warming since 1998[1−5]. Possible explanations for this "warming hiatus" include internal climate variability[3,4,6,7], external cooling influences[1,2,4,8−11], and observational errors[12,13]. One contributory factor to the relatively muted surface warming – early 21st century volcanic forcing – has been examined in several modelling studies[1,2,4,8]. Here we present the first analysis of the impact of recent volcanic forcing on tropospheric temperature, and the first observational assessment of the significance of early 21st century volcanic signals. We identify statistically significant signals in the correlations between stratospheric aerosol optical depth and satellite-based estimates of both tropospheric temperature and short-wave fluxes at the top of the atmosphere. We show that climate model simulations without early 21st century volcanic forcing overestimate the tropospheric warming observed since 1998. In two simulations with more realistic volcanic forcing following the 1991 Pinatubo eruption, differences between modelled and observed tropospheric temperature trends over 1998 to 2012 are decreased by up to 15%, with large uncertainties in the size of the effect. Reducing these uncertainties will require better observational understanding of eruption-specific differences in volcanic aerosol properties, and improved representation of these differences in model simulations.

Our analysis uses satellite measurements of changes in the temperature of the lower troposphere (TLT) made by Microwave Sounding Units (MSU) on NOAA polar-orbiting satellites[13,14]. Satellite TLT data have near-global, time-invariant spatial coverage; in contrast, global-mean trends estimated from surface thermometer records can be biased by spatially- and temporally non-random coverage changes[15]. We compare MSU TLT data to synthetic satellite temperatures[3] calculated from simulations performed under phase 5 of the Coupled Model Intercomparison Project (CMIP-5)[16]. These "ALL+8.5" simulations include estimated historical (1850 to 2005) and future (2006 to 2100) changes in combined anthropogenic and natural external forcings (Supplementary Tables 1-3).

Although our primary focus is on the recent "warming hiatus", we also examine volcanically-induced changes in warming rate following the eruptions of El Chichón (April 1982) and Pinatubo (June 1991). Both volcanic events increased stratospheric loadings of liquid-phase sulfate aerosols, leading to stratospheric warming and tropospheric cooling (Supplementary Fig. 1)[17–19]. Stratospheric temperature recovers within 1-2 years after El Chichón and Pinatubo. Because of the large thermal inertia of the ocean, the recovery of tropospheric temperatures is slower (*ca.* 8-10 years)[20,21].

To analyze volcanic contributions to observed changes in warming rates, it is useful to reduce the amplitude of internal noise[20–22]. Our noise reduction strategy involves removing the temperature signal of the El Niño/Southern Oscillation (ENSO), a

leading mode of internal climate variability. ENSO variability is characterized here by a commonly-used index of sea-surface temperature (SST) changes in the eastern equatorial Pacific[23]. We remove ENSO effects from the satellite data and CMIP-5 simulations with an iterative regression-based method, which accounts for correlation between the predictor variables used to estimate ENSO and volcano temperature signals (see Supplementary Figs. 2 and 3 and Supplementary Methods)[20,21].

Removing ENSO markedly improves the agreement between the observed and the model average temperature responses to major volcanic eruptions (*c.f.* Figs. 1A and B). When both ENSO and volcano influences are subtracted, the model and observed temperature residuals have very similar low-frequency changes up to the end of the 20th century (Fig. 1C). After 1999, however, a "warming hiatus" is still apparent in the observed residual TLT time series, but the lower troposphere continues to warm in the CMIP-5 multi-model average.

This difference between modelled and observed warming trends must be partly due to treatment of 21st century volcanic forcing in the CMIP-5 ALL+8.5 simulations[1,2,4]. In the real world, 17 'small' eruptions occurred after 1999[1,24,25] (see Fig. 2A and Supplementary Table 4). The impact of each of these eruptions on the estimated stratospheric aerosol optical depth (SAOD) is an order of magnitude smaller than that of Pinatubo (Supplementary Fig. 4A). The cumulative effect of these successive 21st century eruptions, however, was to increase global-mean SAOD by 4% to 7%

annually from 2000 to 2009[1,24,25]. This increase in SAOD is not included in any of the ALL+8.5 simulations, which assume that SAOD decayed to background values or zero[1,4] by the year 2000.

Over 50% of the larger (VEI $\geq$ 4) 21st century volcanic events occurred in the tropics (Fig. 2A)[24,25]. The largest eruptions appear to have discernible signatures in satellite estimates of the tropical net clear-sky short-wave (SW) radiation at the top of the atmosphere[26] and in the "ENSO removed" tropical TLT data (Figs. 2B,C). The SW signatures arise because volcanic aerosols reflect part of the incoming solar radiation back to space. The increase in tropical net clear-sky SW radiation over January 2001 to December 2012 (by roughly 0.25 W/m^2/decade) is qualitatively consistent with the independently estimated SAOD increase over this period.

Even after statistical removal of ENSO effects, there is still considerable internal variability in tropical TLT (Fig. 2C). We perform two statistical tests to determine whether recent volcanic eruptions have cooling signals that can be discriminated from this residual variability. First, our "individual eruption" tests (Fig. 3A) consider whether there are statistically significant changes in tropical TLT after eight of the larger volcanic eruptions in the Vernier *et al.* SAOD data set[24]. Significance is assessed by comparing the estimated observed cooling signal of each eruption with appropriate null distributions of TLT changes. These "no volcanic signal" distributions were obtained from 10,000 synthetic TLT time series generated by a lag-1

autoregressive statistical model (see Supplementary Methods).

For Pinatubo, the cooling of the tropical lower troposphere is consistently significant at the 1% level for all 12 sets of processing choices (combinations of averaging period for estimating the pre-eruption temperature and post-eruption cooling). The tropical TLT signals of Manam, Tavurvur, and Nabro are significant at the 10% level or better, but only for certain combinations of processing choices. No averaging period choices explored here yield statistically significant cooling after Nevado del Ruiz, Kelut, Sarychev, or Merapi.

Our second test addresses the statistical significance of correlations between SAOD and "ENSO removed" TLT data (Fig. 3B). Because volcanic activity is inherently non-stationary, the correlation $r\{\text{SAOD}, \text{TLT}\}$ between SAOD and TLT is sensitive to the selected analysis period. We account for non-stationarity in $r\{\text{SAOD}, \text{TLT}\}$ using a 60-month 'moving window' analysis. As in the case of the cooling signals of individual eruptions, we assess the significance of $r\{\text{SAOD}, \text{TLT}\}$ by generating null distributions of this statistic (see Supplementary Methods).

The most significant negative values of $r\{\text{SAOD}, \text{TLT}\}$ occur during 60-month periods which encompass the pronounced SAOD increase and TLT decrease after Pinatubo (Fig. 3B). Moving windows which sample the post-2004 SAOD and TLT changes also yield statistically significant $r\{\text{SAOD}, \text{TLT}\}$ values (at the 10% level or better). Taken together, the results from our "individual eruption" and $r\{\text{SAOD}, \text{TLT}\}$ tests suggest

that internally generated variability could plausibly explain some of the observed tropical TLT changes after individual 'small' eruptions, but is less likely to explain the observed synchronicity between multiple 21st century eruptions and multiple tropospheric cooling signals.

We also calculate $r\{\text{SAOD}, \text{SW}\}$, the contemporaneous correlations between overlapping 60-month segments of observational SAOD and net clear-sky SW radiation time series. For the tropical SAOD and SW changes in the early 21st century, values of $r\{\text{SAOD}, \text{SW}\}$ consistently attain significance at the 5% level or better (Fig. 3B), providing independent confirmation of the $r\{\text{SAOD}, \text{TLT}\}$ results. Our findings for near-global changes in SAOD, TLT, and SW (Supplementary Fig. 5) are similar to those shown here for the tropics.

To better understand the contributions of late 20th and early 21st century volcanic forcing to global-scale changes in tropospheric warming rates, we calculate maximally-overlapping 10-year trends from the "ENSO removed" TLT time series in Fig. 1B. This simple smoothing procedure[3] reveals that observed and model average TLT changes are remarkably similar, both in phase and in amplitude, for the first 20 years of the satellite record (Fig. 4). In contrast, model 10-year TLT trends are larger than observed for trends with start dates after 1993.

The twin trend maxima in Fig. 4 are related to the temperature responses to El Chichón and Pinatubo. Each eruption is followed by a 13- to 14-month cooling phase

until maximum monthly-mean cooling ($\Delta T_{\rm max}$) is attained (Fig. 1C). Tropospheric warming during the slow recovery from El Chichón and Pinatubo augments the more gradual warming trend arising from human-caused increases in greenhouse gases. This is why 10-year TLT trends which begin close to the time of $\Delta T_{\rm max}$ have large positive values. These results clearly show that El Chichón and Pinatubo had important impacts on decadal changes in warming rates, despite statements to the contrary[27].

It has been claimed that the recent divergence between modelled and observed temperature changes provides evidence that CMIP-5 models are (on average) 2-3 times too sensitive to human-caused changes in greenhouse gases[28]. If this claim is correct, there is a serious error in current model-based estimates of the Transient Climate Response (TCR) to greenhouse-gas forcing. Since both TCR and the volcanic signal decay time τ (see Methods) are related to the rate of ocean heat uptake[20], a large model error in ocean heat uptake would yield errors in the simulated temperature response to El Chichón and Pinatubo. The close agreement we find between the observed and model average TLT responses to El Chichón and Pinatubo (see Fig. 4) does not support the claim of a fundamental model error in climate sensitivity.

Based on the results presented here, we argue that the divergence of modelled and observed low-frequency TLT changes over the final 15 years of the satellite record is partly due to systematic errors in the post-Pinatubo volcanic forcing in the ALL+8.5 simulations. Three model-based studies[1,2,8] find that the inclusion of more realistic

post-Pinatubo volcanic forcing reduces global-mean surface temperature by 0.02 to 0.07°C by 2010. We obtain qualitatively similar results (see Supplementary Fig. 6). We analyzed simulations with improved representation of the observed SAOD changes after Pinatubo ("ALL+Vol21c"). These were performed with the `GISS-E2-R` and `CanESM2` models developed at the Goddard Institute for Space Studies and Canadian Centre for Climate Modelling and Analysis (respectively).

After ENSO removal, the discrepancy between the observed TLT trends over 1998 to 2012 and the corresponding trends in the ALL+Vol21c ensemble averages is reduced by 2-4% (`GISS-E2-R`) or by 11-15% (`CanESM2`), depending on which observational data set is selected. These estimates vary because of model differences in: 1) the imposed post-Pinatubo SAOD changes, and whether SAOD is allowed to decay back to near-zero after Pinatubo (see Supplementary Fig. 4A); 2) the decisions made in translating SAOD changes into volcanic aerosol forcing; 3) TCR and equilibrium climate sensitivity; 4) the amplitude and phase of internal climate variability; and 5) the treatment of other (non-volcanic) external forcings.

Better quantification of the contribution of recent volcanic forcing to the "warming hiatus" will require new model simulations, and more detailed analysis of the seasonal and regional attributes of modelled and observed temperature changes. New simulations should involve multiple models and volcanic forcing estimates, larger ensemble sizes, and more detailed examination of the sensitivity to eruption-specific differences

in the radiative properties, horizontal and vertical dispersion, and size distributions of 21st century volcanic aerosols.

In conclusion, we note that systematic forcing errors in CMIP-5 simulations of historical climate change are not confined to the treatment of volcanic aerosols. Errors are also likely to exist in the treatment of recent changes in solar irradiance[9], stratospheric water vapor[10], stratospheric ozone[29,30], and anthropogenic aerosols[11]. Even a hypothetical 'perfect' climate model, with perfect representation of all the important physics operating in the real-world climate system, will fail to capture the observed evolution of climate change if key anthropogenic and natural forcings are neglected or inaccurately represented. It is not scientifically justifiable to claim that model climate sensitivity errors are the only explanation for differences between model and observed temperature trends. Understanding the causes of these differences will require more reliable quantification of the relative contributions from model forcing and sensitivity errors, internal variability, and remaining errors in the observations.

Methods

We use observational TLT results from Remote Sensing Systems in California (RSS; ref. 13, http://www.remss.com/data/msu/data) and the University of Alabama at Huntsville (UAH; ref. 14, http://vortex.nsstc.uah.edu/data/msu). Model TLT data are from ALL+8.5 simulations performed with 28 different CMIP-5 models (Supplementary Tables 1-3). Six of these models have multiple realizations of the ALL+8.5 simulation, yielding a total of 41 realizations of externally forced TLT changes over 1979 to 2012. Model simulation output used in the calculation of synthetic TLT information was downloaded from a portal of the Earth System Grid Federation (http://pcmdi9.llnl.gov/). The statistical method used for removing ENSO and volcano signals from modelled and observed tropospheric temperature data is described in ref. 20 and ref. 21. Application of this approach requires an index characterizing ENSO variability. Here, the selected index was the spatial average of SST changes over the Niño 3.4 region, which was computed from version 3b of the NOAA Extended Reconstructed Sea Surface Temperature dataset (ref. 23, http://www.ncdc.noaa.gov/oa/climate/research/sst) and from the CMIP-5 ALL+8.5 simulations. The SAOD data in Figs. 2A and 3 are an updated version of information published in ref. 24. The Clouds and Earth's Radiant Energy System (CERES) net clear-sky SW radiation data plotted in Fig. 2B are available at http://ceres-tool.larc.nasa.gov/ord-tool/, and are documented in ref. 26. All TLT results shown

in main text Figures (except in Fig. 1A, which gives 'raw' TLT results) rely on TLT data from which ENSO-induced variability was statistically removed with a volcanic signal decay time of $\tau = 40$ months. The Supplementary Methods section provides a full description of: 1) all observational and model TLT data sets used here; 2) the statistical method for removing ENSO-induced TLT variability; 3) the tests applied to assess the statistical significance of volcanically-induced signals in observational TLT and SW data; and 4) details of the `CanESM2` and `GISS-E2-R` Vol21c simulations.

References

1. Solomon, S., Daniel, J. S., Neely, R. R., Vernier, J. P., Dutton, E. G. & Thomason, L. W. The persistently variable "background" stratospheric aerosol layer and global climate change. *Science* **333**, 866-870 (2011).

2. Fyfe, J. C., von Salzen, K., Cole, J. N. S., Gillett, N. P. & Vernier, J.-P. Surface response to stratospheric aerosol changes in a coupled atmosphere-ocean model. *Geophys. Res. Lett.* **40**, 584-588 (2013).

3. Santer, B. D. *et al.* Separating signal and noise in atmospheric temperature changes: The importance of timescale. *J. Geophys. Res.* **116**, D22105, doi:10.10 29/2011JD016263 (2011).

4. Fyfe, J. C., Gillett, N. P. & Zwiers F. W. Overestimated global warming over the past 20 years. *Nat. Cli. Change* **3**, 767-769 (2013).

5. Santer B. D. *et al.* Identifying human influences on atmospheric temperature. *Proc. Nat. Acad. Sci.* **110**, 26-33 (2013).

6. Meehl, G. A., Arblaster, J. M., Fasullo, J. T., Hu, A. & Trenberth, K. E. Model-based evidence of deep-ocean heat uptake during surface-temperature hiatus periods. *Nat. Cli. Change* **1**, 360-364 (2011).

7. Kosaka, K. & Xie, S.-P. Recent global-warming hiatus tied to equatorial Pacific surface cooling. *Nature*, **501**, 403-407 (2013).

8. Haywood, J. M., Jones, A. & Jones, G. S. The impact of volcanic eruptions in the period 2000-2013 on global mean temperature trends evaluated in the HadGEM2-ES climate model. *Atmos. Sci. Lett*, doi:10.1002/asl2.471 (2013).

9. Kopp, G. & Lean, J. L. A new, lower value of total solar irradiance: Evidence and climate significance. *Geophys. Res. Lett.* **38**, L01706, doi:10.1029/2010GL045777 (2011).

10. Solomon, S., Rosenlof, K. H., Portman, R. W., Daniel, J. S., Davis, S. M., Sanford, T. J. & Plattner, G.-K. Contributions of stratospheric water vapor to decadal changes in the rate of global warming. *Science* **327**, 1219-1223 (2010).

11. Shindell, D. T. *et al.* Radiative forcing in the ACCMIP historical and future climate simulations. *Atmos. Chem. Phys.* **13**, 2939-2974 (2013).

12. Morice, C. P., Kennedy, J. J., Rayner, N. A. & Jones, P. D. Quantifying uncertainties in global and regional temperature change using an ensemble of observational estimates: The HadCRUT4 data set. *J. Geophys. Res.* **117**, D08101, doi:10.1029/2011JD017187 (2012).

13. Mears, C., Wentz, F. J., Thorne, P. & Bernie, D. Assessing uncertainty in estimates of atmospheric temperature changes from MSU and AMSU using a Monte-Carlo technique. *J. Geophys. Res.* **116**, D08112, doi:10.1029/2010JD014954 (2011).

14. Christy, J. R., Norris, W. B., Spencer, R. W. & J. J. Hnilo. Tropospheric temperature change since 1979 from tropical radiosonde and satellite measurements. *J. Geophys. Res.* **112**, D06102, doi:10.1029/2005JD006881 (2007).

15. Cowtan, K. & Way, R. G. Coverage bias in the HadCRUT4 temperature series and its impact on recent temperature trends. *Quart. J. Roy. Met. Soc.* (in press; doi:10.1002/qj.2297).

16. Taylor, K. E., Stouffer, R. J. & Meehl, G. A. An overview of CMIP5 and the experiment design. *Bull. Amer. Meteor. Soc.* doi:10.1175/BAMS-D-11-00094.1 (2012).

17. Robock, A. Volcanic eruptions and climate. *Rev. Geophys.* **38**, 191-219 (2000).

18. Sato, M., Hansen, J. E., McCormick, M. P. & Pollack, J. B. Stratospheric aerosol optical depth, 1850-1990. *J. Geophys. Res.* **98**, 22987-22994 (1993).

19. Ramaswamy, V., Schwarzkopf, M. D., Randel, W. J., Santer, B. D., Soden, B. J. & Stenchikov, G. L. Anthropogenic and natural influences in the evolution of lower stratospheric cooling. *Science* **311**, 1138-1141 (2006).

20. Wigley, T. M. L., Ammann, C. M., Santer, B. D. & Raper, S. C. B. The effect of climate sensitivity on the response to volcanic forcing. *J. Geophys. Res.* **110**, D09107, doi:10.1029/2004/JD005557 (2005).

21. Santer, B. D. *et al.* Accounting for the effects of volcanoes and ENSO in com-

parisons of modeled and observed temperature trends. *J. Geophys. Res.* **106**, 28033-28059 (2001).

22. Thompson, D. W. J., Wallace, J. M., Jones, P. D. & Kennedy, J. J. Identifying signatures of natural climate variability in time series of global-mean surface temperature: Methodology and insights. *J. Clim.* **22**, 6120-6141 (2009).

23. Smith, T. M., Reynolds, R. W., Peterson, T. C. & Lawrimore, J. Improvements to NOAA's historical merged land-ocean surface temperature analysis (1880-2006). *J. Clim.* **21**, 2283-2296 (2008).

24. Vernier, J.-P. *et al.* Major influence of tropical volcanic eruptions on the stratospheric aerosol layer during the last decade. *Geophys. Res. Lett.* **38**, L12807, doi:10.1029/2011GL047563 (2011).

25. R. R. Neely III *et al.* Recent anthropogenic increases in SO_2 from Asia have minimal impact on stratospheric aerosol. *Geophys. Res. Lett.* **40**, doi:10.1002grl.50263 (2013).

26. Loeb, N. G. *et al.* Towards optimal closure of the earth's top-of-atmosphere radiation budget. *J. Climate* **22**, 748-766 (2009).

27. Muller, R. http://www.nytimes.com/2013/09/26/opinion/a-pause-not-an-end-to-warming.html?_r=0.

28. J. R. Christy, Testimony in Hearing before the Subcommittee on Energy and

Power, Committee on Energy and Commerce, House of Representatives, March 8, 2011. See http://republicans.energycommerce.house.gov/Media/file/Hearings/Energy/030811/Christy.pdf

29. Hassler, B. *et al.* Comparison of three vertically resolved ozone data sets: climatology, trends and radiative forcings. *Atmos. Chem. Phys.* **13**, 5533-5550 (2013).

30. Eyring, V. *et al.* Long-term ozone changes ozone and associated climate impacts in CMIP5 simulations. *J. Geophys. Res.* **118**, 5029-5060 (2013).

Acknowledgements

We acknowledge the World Climate Research Programme's Working Group on Coupled Modelling, which is responsible for CMIP, and we thank the climate modelling groups for producing and making available their model output. For CMIP, the U.S. Department of Energy's Program for Climate Model Diagnosis and Intercomparison (PCMDI) provides coordinating support and led development of software infrastructure in partnership with the Global Organization for Earth System Science Portals. Jean-Paul Vernier (NASA Langley) and Makiko Sato (GISS) supplied updated SAOD data. Tom Wigley (Univ. of Adelaide), Nathan Gillett (Canadian Centre for Climate Modelling and Analysis), Alan Robock (Rutgers Univ.), Kevin Trenberth (National Center for Atmospheric Research), and Simon Tett (Univ. of Edinburgh) provided helpful comments. At PCMDI, work by B.D.S., J.P., M.Z., and K.E.T. was performed under the auspices of the U.S. Department of Energy under contract DE-AC52-07NA27344; C.B. was supported by the DOE/OBER Early Career Research Program Award SCW1295.

Author Contributions

B.D.S., C.B., M.Z., C.M., S.S., G.A.S., J.C.F., and K.E.T. designed the analysis of model simulations and observational data. B.D.S., C.B., and M.Z. performed the analysis. G.A.S., J.C.F., J.N.S.C., and L.N. designed, completed, and analyzed the Vol21c integrations. J.P. calculated synthetic MSU temperatures. C.M. and F.J.W.

contributed MSU temperature data. All authors wrote the manuscript.

Author Information

Correspondence and requests for materials should be addressed to B.D.S. (santer1@llnl.gov).

Figure 1: Modelled and observed near-global (82.5°N-70°S) monthly-mean TLT anomalies before and after statistical removal of ENSO and volcano signals. The original TLT anomalies (panel A) are departures from the climatological monthly means over January 1979 to December 2012. Removal of the estimated ENSO signal in TLT reduces the noise which partially obscures the temperature response to the eruptions of El Chichón and Pinatubo (panel B). Subtraction of the ENSO, El Chichón, and Pinatubo signals from the original TLT data yields the temperature residuals in panel C.

Figure 2: Changes in observed SAOD[24] (panel A), net clear-sky SW radiation at the top of the atmosphere[26] (panel B), and "ENSO removed" TLT data[13] (panel C). Results are spatially averaged over the tropics (20°N-20°S). A five-term binomial filter was used to produce the smoothed results (bold lines) in panels B and C. Vertical lines denote the dates of the eruptions listed in Supplementary Table 4. Eruptions which occurred within (outside) the 20°N-20°S latitude band are indicated by solid (dashed) vertical lines.

Figure 3: Statistical significance of observed tropical (20°N-20°S) climate signals after late 20th and early 21st century volcanic eruptions. Panel A shows estimated observed changes in SAOD[24] and "ENSO-removed" TLT[13] (Δ_{SAOD} and Δ_{TLT}) after 8 individual eruptions. For each eruption, there are 36 different combinations of Δ_{SAOD} and Δ_{TLT}, calculated with different lengths of averaging period for determin-

ing pre- and post-eruption changes. Values of Δ_{TLT} within the grey shaded area are statistically significant at the 10% level or better; values below the yellow line are significant at the 1% level. Panel B shows $r\{\mathrm{SAOD,\,TLT}\}$, the lagged correlations between monthly-mean observational time series of SAOD and TLT, and $r\{\mathrm{SAOD,\,SW}\}$, the contemporaneous correlations between SAOD and net clear-sky SW radiation[26]. Values of $r\{\mathrm{SAOD,\,TLT}\}$ and $r\{\mathrm{SAOD,\,SW}\}$ were computed using a 60-month moving window, with overlap of 59 months between successive analysis periods. Since observed SW time series are shorter than TLT records, $r\{\mathrm{SAOD,\,SW}\}$ can only be shown for 60-month periods beginning after 2000. The sign of $r\{\mathrm{SAOD,\,SW}\}$ was changed to facilitate display with $r\{\mathrm{SAOD,\,TLT}\}$ results. The statistical significance of $r\{\mathrm{SAOD,\,TLT}\}$ and $r\{\mathrm{SAOD,\,SW}\}$ is indicated on the alternate y-axis of panel B. The significance tests applied in panels A and B are described in the Supplementary Methods.

Figure 4: Behavior of overlapping 10-year trends in the "ENSO removed" near-global (82.5°N-70°S) TLT data. Least-squares linear trends were calculated over 120 months, with overlap by all but one month; *i.e.*, the first trend is over January 1979 to December 1988, the second trend over February 1979 to January 1989, *etc.* The last trend is over January 2003 to December 2012.

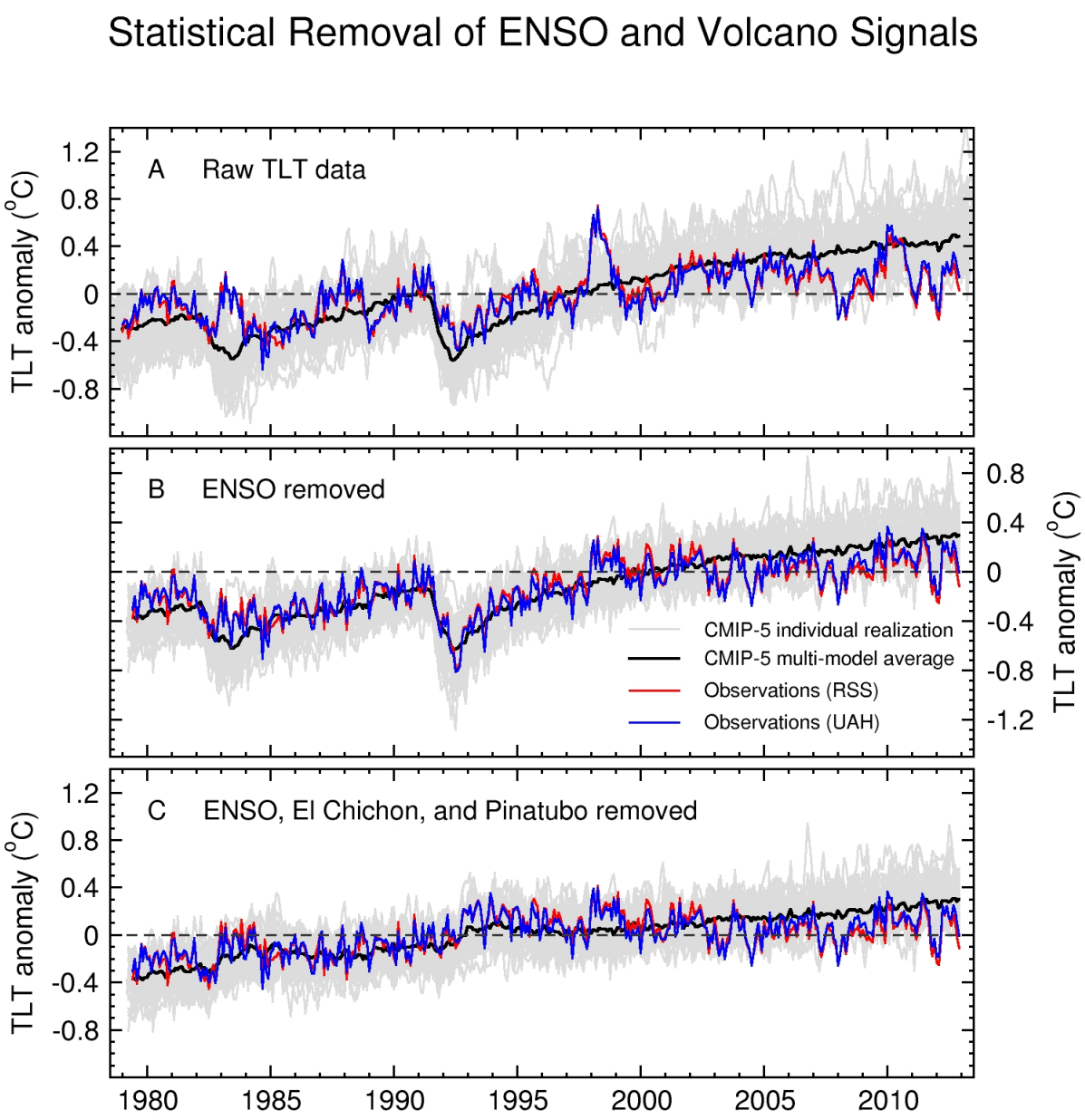

Figure 1: Santer *et al.*

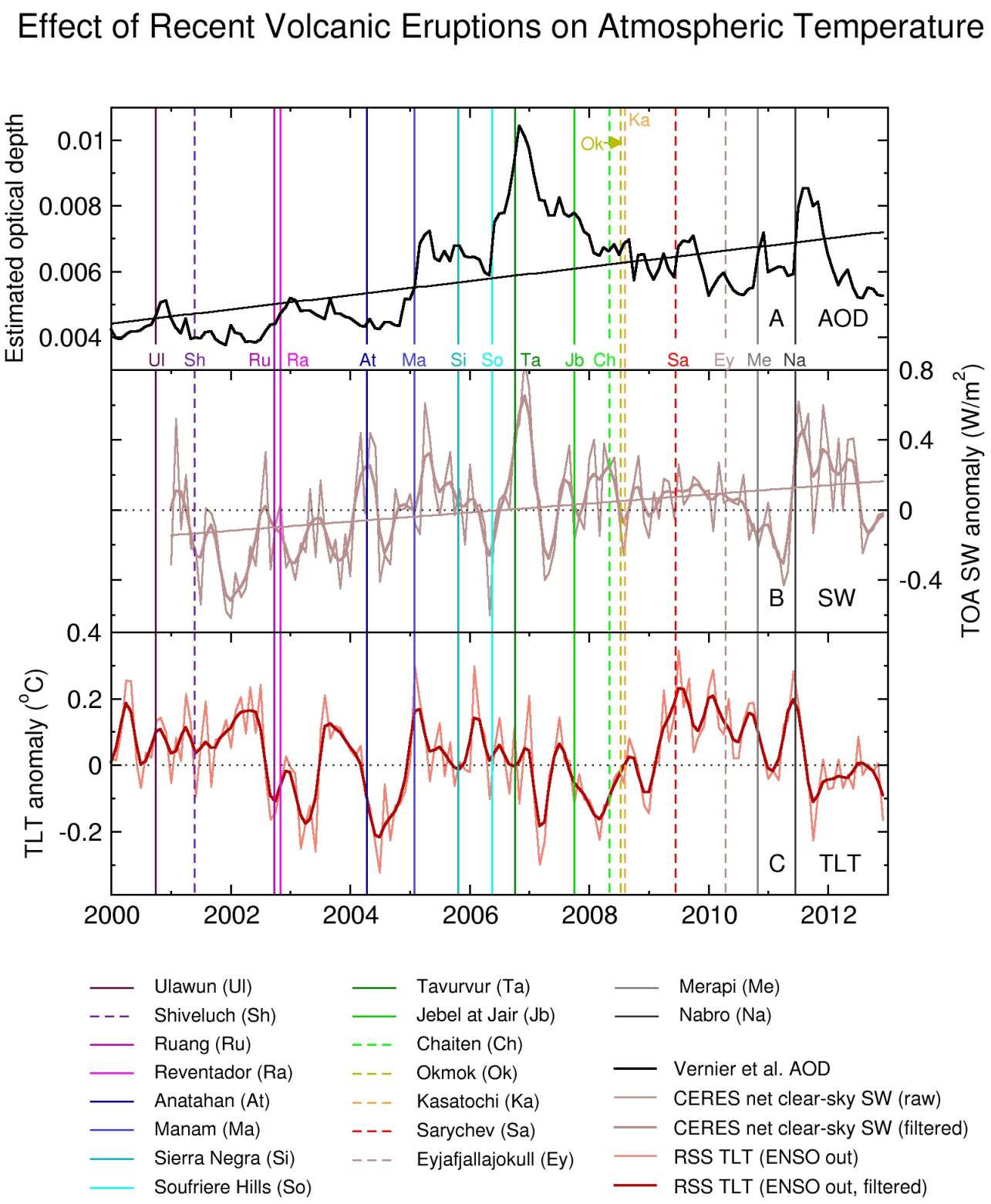

Figure 2: Santer *et al.*

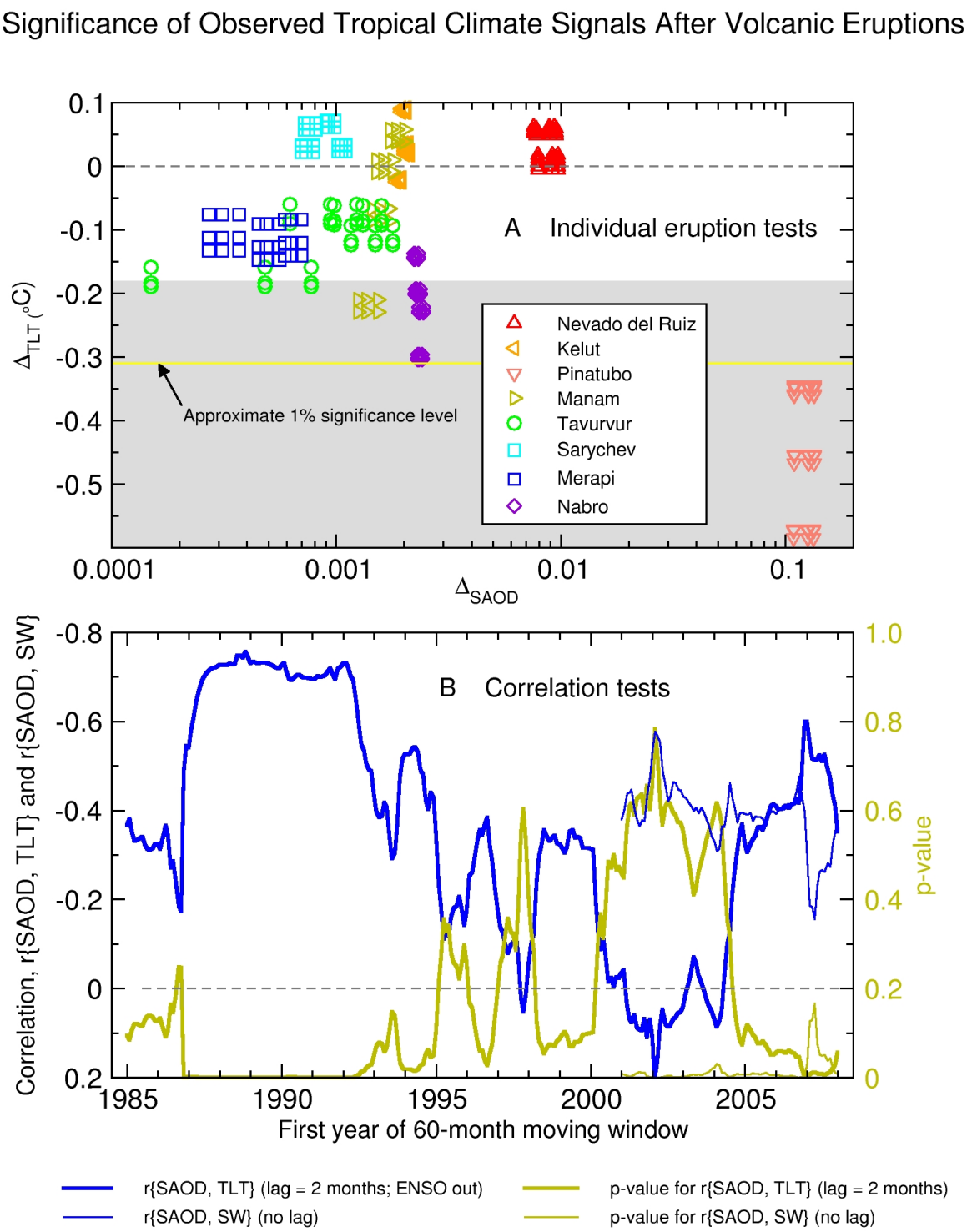

Figure 3: Santer *et al.*

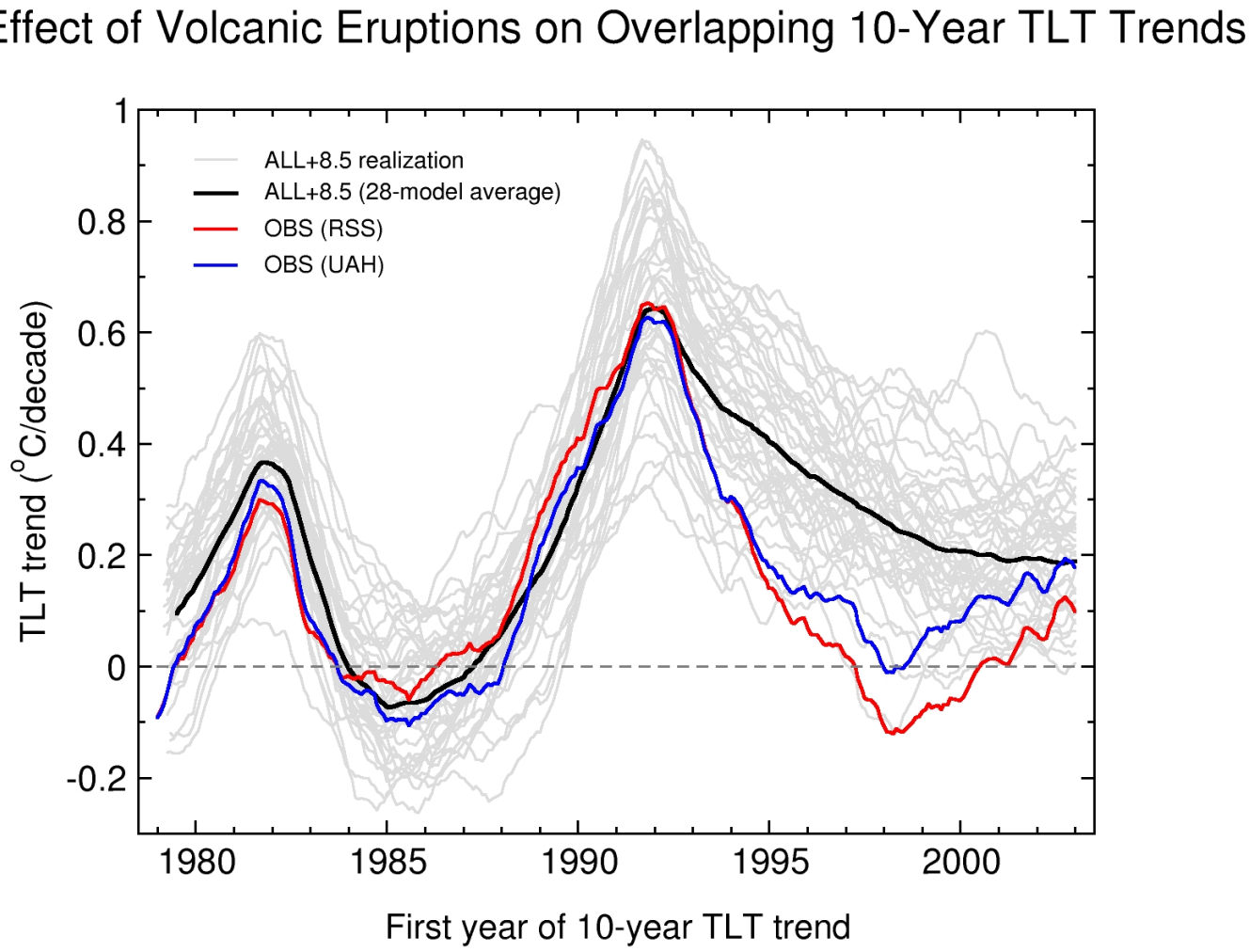

Figure 4: Santer *et al.*

Supplementary Information

1 Observational atmospheric temperature data

We used satellite measurements of atmospheric temperature change produced by RSS (ref. 13) and UAH (ref. 14). Both groups provide MSU-based estimates of vertically weighted, layer-average temperature changes for the temperature of the lower troposphere (TLT) and the temperature of the lower stratosphere (TLS). We analyzed MSU temperatures from data set versions 3.3 (RSS) and 5.5 (UAH). Observed MSU data were in the form of monthly means for the 408-month period January 1979 to December 2012, and are on a 2.5° × 2.5° latitude/longitude grid. RSS and UAH MSU data sets have small differences in spatial coverage at high latitudes (ref. 5). All near-global spatial averages of observed and simulated MSU temperatures were calculated over the area of common coverage in the RSS and UAH data (82.5°N to 70°S for TLT, and 82.5°N to 82.5°S for TLS).

2 Observational sea-surface temperature data

We used data from version 3b of the NOAA Extended Reconstructed Sea Surface Temperature dataset (ERSST) (ref. 23) for calculating spatially-averaged SST changes over the Niño 3.4 region (5°N-5°S; 170°W-120°W). ERSST data were available from January 1854 to December 2012 in the form of monthly means on a regular 2° × 2°

latitude/longitude grid. Further details of the ERSST dataset are available online at http://www.ncdc.noaa.gov/oa/climate/research/sst/ersstv3.php.

3 Observational SAOD data

Observational stratospheric aerosol optical depth (SAOD) measurements were provided by Jean-Paul Vernier (NASA Langley Research Center) and Makiko Sato (NASA Goddard Institute for Space Studies). These are updated versions of the SAOD data sets described in previously published studies (ref. 24 and ref. 18).

3.1 Vernier et al. SAOD

The Vernier monthly-mean SAOD data are in the form of zonal averages for 5° latitude bands, with coverage extending from 50°N-50°S. Data were available for the 336-month period from January 1985 to December 2012. The altitude range of the measurements is 15 to 40 km. Results are from three different sets of satellite-based aerosol measurements: 1) Stratospheric Aerosol and Gas Experiment, phase II (SAGE II; January 1985 to August 2005); 2) Global Ozone Monitoring by Occultation of Stars (GOMOS; September 2005 to May 2006); and 3) Cloud-Aerosol Lidar and Infrared Pathfinder Satellite Observations (CALIPSO; June 2006 to December 2012). Further discussion of these measurements and the SAOD signatures of 21st century volcanic eruptions is given elsewhere (refs. 1, 24, 25, 31).

3.2 Sato et al. SAOD

In the analyses presented in Supplementary Fig. 4A, we used version C of the Sato *et al.* SAOD data, which became available in May 2013. This version includes SAOD information from the satellite-based Optical Spectrograph and Infra-Red Imaging System (OSIRIS). The altitude range of the measurements is 15 to 35 km.

4 Observational SW data

In Fig. 2B, we used Edition 2.7 of the Energy Balance And Filled (EBAF) Clouds and Earth's Radiant Energy System (CERES) net clear-sky SW radiation data (ref. 26). The SW anomalies in Fig. 2B are defined with respect to climatological monthly means computed over the full 154-month period covered by the CERES EBAF data (March 2000 to February 2013, inclusive). We show clear-sky SW results to reduce obfuscating cloud effects. Focusing on net clear-sky SW radiation accounts for the effect of changes in the downwelling component of SW associated with changes in solar irradiance over the 11-year solar cycle.

5 Model simulation output

5.1 ALL+8.5 simulations

We analyze atmospheric temperature changes from CMIP-5 simulations with human, volcanic, and solar external forcings (ALL), and from CMIP-5 integrations with 21st

century changes in greenhouse gases and anthropogenic aerosols specified according to Representative Concentration Pathway 8.5 (RCP8.5). We spliced TLT information from the ALL simulations (which typically end in December 2005) with TLT results from the RCP8.5 runs. Splicing facilitates comparison of modelled and observed lower tropospheric temperature changes over the full observational satellite record. Spliced results are referred to subsequently as "ALL+8.5".

We only consider ALL+8.5 simulations that incorporate the direct radiative effects of the El Chichón and Pinatubo volcanic aerosols. These were available for 28 different CMIP-5 models. Supplementary Tables 1-3 provide information on the models used in our analysis, the applied external forcings in the ALL simulations, the ALL and RCP8.5 start and end dates, and the splicing of the ALL and RCP8.5 runs.

5.1.1 Splicing of ALL and 8.5 temperature data

For 27 of the 28 CMIP-5 models analyzed here, the ALL synthetic MSU temperature changes were spliced together with RCP8.5 results. In the case of `CNRM-CM5`, there is a discontinuity in the volcanic aerosol forcing between the ALL and RCP8.5 simulations. This discontinuity is removed by splicing the `CNRM-CM5` ALL and historicalExt simulations (ref. 5).

5.1.2 Treatment of different GISS-E2-R physics versions

For the `GISS-E2-R` ALL+8.5 simulations, output was available from three different model versions (`p1`, `p2`, and `p3`). In calculating ALL+8.5 multi-model averages, we treated atmospheric temperatures from the `GISS-E2-R` `p1`, `p2` and `p3` ALL+8.5 runs as results from three different models of the climate system rather than as different realizations of climate change performed with a similar physical model (ref. 5).

5.2 Vol21c simulations

For the `GISS-E2-R (p3)` and `CanESM2` models, we also analyze output from integrations with updated post-Pinatubo volcanic aerosol forcing ("Vol21c"), as well as from simulations with 21st century greenhouse gas and anthropogenic aerosol forcing specified according to the RCP4.5 scenario.

5.2.1 GISS-E2-R (p3) simulations with volcanic forcing

The `GISS-E2-R (p3)` ALL+8.5 and ALL+4.5 runs rely on version A of the Sato *et al.* SAOD data set (ref. 18), which was available in 2009. Version A consisted of SAOD measurements spanning the period 1850 to 1999; SAOD was assumed to decay to zero by the end of 20th century[1]. In the `GISS-E2-R (p3)` Vol21c simulation, volcanic forcing is based on version C of Sato *et al.* Relative to version A, version C has more realistic treatment of the estimated observed SAOD changes from 1999 to

[1]Similar assumptions were made in the ALL+8.5 and ALL+4.5 simulations performed with all other CMIP-5 models analyzed here.

2012. The Vol21c simulation also includes updated solar forcing, with representation of the extended solar minimum during the last solar cycle (ref. 9).

Five realizations of the Vol21c simulation were performed. Each realization was spawned from December 1990 conditions of a corresponding `GISS-E2-R (p3)` ALL realization[2]. Relative to the ALL+8.5 simulations, the `GISS-E2-R (p3)` spliced ALL+Vol21c runs differ in terms of their volcanic aerosols (post-1999), greenhouse gases and anthropogenic aerosols (post-2005), and solar irradiance changes (post-2000). The post-2005 changes in greenhouse gases and aerosol precursor emissions in Vol21c are the same as those used in the `GISS-E2-R (p3)` RCP4.5 runs.

We compared the `GISS-E2-R (p3)` ALL+Vol21c results with the corresponding five realizations of the spliced ALL+4.5 runs. Differences between the low-frequency TLT changes in ALL+Vol21c and ALL+4.5 arise because of differences in both volcanic aerosol forcing and solar forcing (see Supplementary Fig. 6A).

[2]We analyzed `GISS-E2-R (p3)` ALL, Vol21c, and RCP4.5 realizations r1i1p3, r2i1p3, r3i1p3, r4i1p3, and r5i1p3. Here, 'corresponding' signifies that Vol21c r1i1p3 and RCP4.5 r1i1p3 were both spawned from the end of the same realization (r1i1p3) of the `GISS-E2-R (p3)` ALL simulation (*etc.*)

5.2.2 CanESM2 simulations with volcanic forcing

The `CanESM2` Vol21c simulations are described in Fyfe *et al.* (ref. 2). Five Vol21c realizations were available[3]; each was initiated from conditions taken from a different `CanESM2` ALL realization on September 1, 1995. Prior to this date, the `CanESM2` ALL realizations used version A of the Sato *et al.* volcanic aerosol forcing (see section 6.1). From September 1995 to 2011, SAOD was prescribed according to Vernier *et al.* (ref. 24). After 2011, it was assumed that SAOD increased by 5% per year[4].

As in the case of the `GISS-E2-R (p3)` model, the greenhouse gas and anthropogenic aerosol forcings in the `CanESM2` Vol21c simulation were specified according to RCP4.5. The comparison between the ALL+Vol21c and ALL+4.5 results isolates the impact of 'updated' volcanic aerosol forcing on TLT[5]. The `CanESM2` ALL+4.5 (and ALL+8.5) simulations use the 'original' (version A) Sato *et al.* volcanic aerosol forcing, with an assumed decay of SAOD to near-zero values by the year 2000 (ref. 18).

[3]We analyzed five realizations (r1i1p1, r2i1p1, r3i1p1, r4i1p1, and r5i1p1) for each of the three `CanESM2` numerical experiments (ALL, Vol21c, and RCP4.5).

[4]The 'updated' Vernier *et al.* SAOD estimates used here are slightly different from the Vernier *et al.* (2011) SAOD data used in the `CanESM2` Vol21c simulations.

[5]Unlike the `GISS-E2-R (p3)` simulations described above, the `CanESM2` ALL+Vol21c and ALL+4.5 runs do not differ in terms of their solar forcing.

6 Estimation of Equilibrium Climate Sensitivity

For the removal of volcano signals in the "ECS" case in Supplementary Fig. 3, it is necessary to compute the equilibrium climate sensitivity (ECS) of individual CMIP-5 models. ECS is calculated following a standard methodology (ref. 33), which is based on a global mean energy budget framework (ref. 34). This framework expresses the planetary energy budget as:

$$\Delta N = F - \alpha \Delta T \tag{1}$$

where ΔN and ΔT are anomalies[6] in global mean top of the atmosphere net radiation and surface air temperature, respectively. By regressing ΔN on ΔT, we obtain estimates of the adjusted radiative forcing F (the y-intercept) and the net feedback α (the slope of the regression).

Because the $4\times CO_2$ simulations analyzed here are not of sufficient length to achieve true equilibrium with the $4\times CO_2$ forcing (at which time ΔN would equal zero), we estimate ECS as F/α. As is common practice, we divide these ECS values by 2 to obtain the equivalent estimate for a doubling of CO_2. The ECS results calculated here are in close agreement with those derived by (ref. 33), differing by less than 2% for each model.

[6]Anomalies are defined as differences between an abrupt $4\times CO_2$ simulation and a corresponding pre-industrial control run.

7 Removal of ENSO and volcano signals

The method we use for statistical removal of ENSO and volcano signals from observational and model TLT and TMT data is described in detail elsewhere (refs. 20, 21). We provide a brief summary of the method below.

7.1 Method

Let T_t represent monthly-mean TLT data, spatially averaged over a selected domain, and X_t denote some specified index of ENSO variability. The nominal time index is $t = 1, \ldots, n_t$, with $n_t = 408$ in all of our applications (January 1979 through December 2012). Both T_t and X_t are in the form of anomalies with respect to their climatological monthly means over the full 408-month period.

Step 1: Select X_t, T_t, and a value of the volcanic signal decay time τ. Values of τ depend on both ocean thermal inertia and the Equilibrium Climate Sensitivity (ECS) (ref. 20). It is difficult to estimate τ reliably from observations, because the long 'tail' of the volcanic signal is obscured by monthly and interannual noise, and by the temperature responses to slowly-varying non-volcanic forcings (refs. 20-22).

Here, we perform volcano signal removal in two ways: 1) using four different stipulated values of τ; and 2) with τ values calculated from the individual equilibrium climate sensitivities of 22 CMIP-5 models. The stipulated values of τ are 30, 35, 40, and 45 months, which correspond to sensitivities of approximately 1.0, 2.0, 3.5, and 5.8°C

(respectively). To compute τ for individual models, we use the relationship given in Wigley *et al.* (ref. 20), which was derived with an upwelling-diffusion energy balance model:

$$\tau = 30(\Delta T_{2\times})^{0.23} \tag{2}$$

where $\Delta T_{2\times}$ is the ECS for a doubling of pre-industrial atmospheric CO_2.

Step 2: As a function of the lag k (in months) between X_t and T_t, compute the least-squares linear regression coefficient b_k between the selected ENSO index X_t and the tropospheric temperature time series T_t:

$$b_k = \frac{\sum_{t=1}^{n_t-k} \left[(X_t - \overline{X})(T_{t+k} - \overline{T}) \right]}{\sum_{t=1}^{n_t-k} (X_t - \overline{X})^2} \qquad k = 0, \ldots, 24 \tag{3}$$

where $\overline{X}$ and $\overline{T}$ are the time-means of X_t and T_t, respectively. Then determine the lag j (in months) that maximizes $|b_k|$, with $0 \leq j \leq 24$. For observed TLT data, j is typically 3 months for tropical averages (20°N-20°S) and 5 months for near-global averages. Most CMIP-5 models yield similar lag estimates.

Step 3: Compute the linear influence of X_t on T_t:

$$E_{t+j} = a_j + b_j \, X_t \qquad t = 1, \ldots, n_t - j \tag{4}$$

where a_j is the regression estimate of the y-axis intercept at lag j.

Step 4: Subtract the ENSO effect from the raw temperature data:

$$Z_t = T_t - E_t \qquad t = j+1, \ldots, n_t \tag{5}$$

Step 5: For each of the two volcanic eruptions considered (Pinatubo and El Chichón), use the 'ENSO removed' Z_t data to estimate $T_{\rm ref}$, the pre-eruption reference level temperature. $T_{\rm ref}$ is the average Z_t value over the $t_{\rm base}$ months prior to the eruption. We considered $t_{\rm base}$ values of 4 and 6 months. All of the results shown in the main text are for $t_{\rm base} = 6$ months. Note that $T_{\rm ref}$ is calculated using either smoothed or unsmoothed data (see Step 6).

Step 6: Estimate the volcano parameters $\Delta T_{\rm max}$ and $t_{\rm ramp}$ from the 'ENSO removed' Z_t data. The maximum cooling $\Delta T_{\rm max}$ is:

$$\Delta T_{\rm max} = T_{\rm ref} - T_{t_{\rm ramp}} \tag{6}$$

where $t_{\rm ramp}$ is the time (in months since the eruption month) at which $\Delta T_{\rm max}$ occurs. Here, we use $t_{\rm ramp} \leq 24$, which restricts the search for $\Delta T_{\rm max}$ and $t_{\rm ramp}$ to the 24 months following each eruption. Larger values of $t_{\rm ramp}$ are physically unrealistic.

We estimate $\Delta T_{\rm max}$ and $t_{\rm ramp}$ from both unsmoothed and smoothed values of Z_t. In the presence of substantial high-frequency noise, it is useful to perform some degree of smoothing prior to calculation of $\Delta T_{\rm max}$ and $t_{\rm ramp}$. We experimented with a variety of filters and cutoffs, but report only on the results obtained with a five-term binomial

filter. Filters with much longer cutoffs can yield excessive smoothing, and hence to underestimation of $\Delta T_{\max}$.

Step 7: Compute the volcano signal V_t, assuming linear cooling from the eruption month to $t_{\rm ramp}$ and exponential recovery thereafter:

$$\begin{aligned} V_t &= \frac{-\Delta T_{\max}\, t}{t_{\rm ramp}} \qquad\qquad t = t_1, \ldots, t_{\rm ramp} \\ &= -\Delta T_{\max}\, e^{-\frac{t - t_{\rm ramp}}{\tau}} \qquad t > t_{\rm ramp} \end{aligned} \tag{7}$$

Step 8: Subtract the volcano signal from T_t, the original temperature data:

$$T_t^* = T_t - V_t \qquad t = t_1, \ldots, n_t \tag{8}$$

Step 9: Return to Step 2, but now operate on T_t^* rather than on the original temperature data, T_t. Continue iterating until there is convergence of the estimated volcano parameters and b_j. Convergence generally occurs within 4-5 iterations. All results presented here are for 10 iterations. The order in which ENSO and volcano effects are removed from T_t is generally irrelevant as long as sufficient iterations are performed.

Step 10: At the end of the iterative procedure, we subtract our final estimates of the ENSO and volcano signals from the original temperature data, yielding residuals ε_t:

$$\varepsilon_t = T_t - V_t - E_t \qquad t = j+1, \ldots, n_t \tag{9}$$

8 Statistical significance of volcanic signals

We seek to assess the statistical significance of the observational results presented in Fig. 3 and in Supplementary Fig. 5. This involves addressing two different statistical questions. First, we identify 8 of the largest late 20th and early 21st century volcanic eruptions, and consider whether the TLT changes after each of these individual eruptions can be discriminated from the background noise of residual internally generated variability (*i.e.*, the noise remaining after statistical removal of ENSO-induced fluctuations in TLT). Second, we evaluate whether large negative values of correlations between 60-month segments of SAOD and TLT time series are statistically significant, or could be due to residual noise alone. We also consider whether the large positive correlations between 60-month segments of SAOD and SW time series are statistically significant[7].

8.1 Significance tests for individual eruptions

Our significance testing strategy involves use of a standard lag-1 autoregressive statistical model (AR-1) to generate synthetic observational TLT time series:

$$x(t) = a_1 x(t-1) + z(t) \quad ; \; t = 1, \ldots, n_t \tag{10}$$

[7]In other words, whether there is a significant relationship between volcanically-induced increases in SAOD and increases in net clear-sky SW radiation at the top of the atmosphere.

where $x(t)$ is a single realization of synthetic TLT data, a_1 is the coefficient of the AR-1 model, and $z(t)$ is randomly-generated white noise (see ref. 35).

Here, we estimated a_1 from the "ENSO removed" RSS TLT data during the 84-month volcanically-quiescent period from January 1998 to December 2004 (see Supplementary Fig. 4). The noise $z(t)$ in equation (10) was scaled so that the temporal standard deviation of $x(t)$ is approximately the same as that of the RSS residual TLT data during the volcanically-quiescent period mentioned above.

We generate 10,000 different realizations of $x(t)$. For each realization, and for each of the 8 selected eruptions in Fig. 3A, we calculate $\Delta_{\rm TLT}$, the post-eruption change in TLT. To estimate $\Delta_{\rm TLT}$, we difference the time averages over some specified number of months before and after the eruption. Time averaging damps some of the residual monthly variability which hampers reliable estimation of $\Delta T_{\rm max}$.

Many different choices are possible for the number of months over which pre- and post-eruption temperatures are calculated ($n_{\rm ref}\{{\rm TLT}\}$ and $n_{\rm vol}\{{\rm TLT}\}$, respectively). Here, we explore the following choices:

$$\begin{aligned} n_{\rm ref}\{{\rm TLT}\} &= 1, 2, 3, 4; \\ n_{\rm vol}\{{\rm TLT}\} &= 5, 6, 7 \end{aligned}$$

This yields 12 $\Delta_{\rm TLT}$ estimates for each eruption. TLT values for the eruption month itself are used in computing the pre-eruption reference level temperature. Calculations of the post-eruption temperature changes only use data after the eruption month.

For $n_{\rm ref}\{\rm TLT\} = 1$, no time average is calculated, and the pre-eruption reference level temperature is simply the TLT anomaly for the eruption month[8].

The maximum value of $n_{\rm vol}\{\rm TLT\}$, 7 months, is dictated by the close temporal proximity of the Merapi and Nabro eruptions. Nabro erupted in June 2011, roughly 7.5 months after the eruption of Merapi (see Supplementary Table 4). For values of $n_{\rm vol}\{\rm TLT\}$ greater than 7 months, the estimated $\Delta_{\rm TLT}$ signal for Merapi would sample some of the cooling caused by Nabro[9].

The observed values of $\Delta_{\rm TLT}$ are calculated in an analogous way, and are then compared (for each of the 8 eruptions considered, and for each of the 12 averaging period combinations) with the corresponding sampling distribution of 10,000 synthetic values of TLT changes. This allows us to compute empirical p-values for tests of the null hypothesis that residual internal variability alone could explain the observed values of $\Delta_{\rm TLT}$. Values of $\Delta_{\rm TLT}$ estimated from the synthetic time series are Normally distributed, with mean zero. On average, therefore, the likelihood of "observing" post-eruption cooling in a synthetic time series (*i.e.*, of obtaining a negative value of $\Delta_{\rm TLT}$) is the same as the likelihood of "observing" warming after an eruption.

[8]Note that if an eruption occurs within 5 days of the end of a given month, the month following the eruption is designated as the eruption month. This is the case with two of the 8 eruptions we analyzed in Fig. 3A and Supplementary Fig. 5A (Manam and Merapi, which erupted on Jan. 27, 2005, and Oct. 26th, 2010, respectively).

[9]Because of the small period of time between Soufrière Hills and Tavurvur (less than 5 months) the former eruption was excluded from the analysis in Fig. 3A and Supplementary Fig. 5A.

The grey shaded areas in Fig. 3A and Supplementary Fig. 5A provide information on the statistical significance of the observed $\Delta_{\rm TLT}$ results. Symbols within the shaded area denote eruptions (and combinations of $n_{\rm ref}\{{\rm TLT}\}$ and $n_{\rm vol}\{{\rm TLT}\}$) with lower tropospheric cooling that is statistically significant at the 10% level or better. Given the large number of realizations, the null distributions of $\Delta_{\rm TLT}$ are virtually identical for different eruptions, but can show small differences for different pre- and post-eruption averaging period choices. This is why the upper boundary of the shaded region in Fig. 3A and Supplementary Fig. 5A is approximate. In practice, all observed $\Delta_{\rm TLT}$ results with p-values < 0.1 (and no observed $\Delta_{\rm TLT}$ results with p-values > 0.1) are within the shaded region.

The $\Delta_{\rm SAOD}$ changes in Fig. 3A and Supplementary Fig. 5A were calculated with the following averaging period choices (in months):

$$\begin{aligned} n_{\rm ref}\{{\rm SAOD}\} &= 1, 2, 3, 4; \\ n_{\rm vol}\{{\rm SAOD}\} &= 3, 4, 5 \end{aligned}$$

Because SAOD decays more rapidly than TLT after a volcanic eruption, we chose values of $n_{\rm vol}\{{\rm SAOD}\}$ that are smaller than all but one of the $n_{\rm vol}\{{\rm TLT}\}$ averaging period choices.

8.2 Significance tests of correlation coefficients

8.2.1 SAOD and TLT

We generate 10,000-member null distributions of $r\{\text{SAOD}, \text{TLT}\}$ (the correlations between the observed SAOD and "ENSO removed" TLT data) using the synthetic TLT time series described in the previous section. We calculate both contemporaneous correlations and correlations with "ENSO removed" TLT lagging SAOD by either one or two months. Because of the lag between volcanic forcing and the temperature response of the bulk tropical or near-global troposphere, values of $r\{\text{SAOD}, \text{TLT}\}$ during volcanically active periods are typically larger (*i.e.*, more negative) for lagged than for contemporaneous comparisons. We show only the two-month lagged $r\{\text{SAOD}, \text{TLT}\}$ results in Fig. 3B and Supplementary Fig. 5B.

Synthetic TLT data are processed in the same way as the observational results: correlations are computed with overlapping 60-month segments of the observed SAOD and synthetic TLT time series. This yields a separate null distribution of $r\{\text{SAOD}, \text{TLT}\}$ for each of the 60-month segments, and separate null distributions for the contemporaneous and lagged results. We then compare the observed $r\{\text{SAOD}, \text{TLT}\}$ values with the appropriate null distribution, and estimate empirical p-values (shown on the alternate y-axis of Fig. 3B and Supplementary Fig. 5B).

8.2.2 SAOD and SW radiation

Assessment of statistical significance is very similar for values of $r\{\text{SAOD}, \text{SW}\}$. There are three differences relative to the significance assessment for $r\{\text{SAOD}, \text{TLT}\}$ results. First, since the CERES SW radiation record commences in March 2000 (ref. 26), we use the shorter 48-month volcanically-quiescent period from January 2001 to December 2004 for calculating a_1 and scaling the noise $z(t)$ in equation (10). Second, since ENSO explains $< 5\%$ of the temporal variance of the CERES net clear-sky SW radiation data, ENSO effects were not removed from the CERES SW time series prior to estimating a_1 and scaling $z(t)$. Third, because net clear-sky SW radiation at the top of the atmosphere responds very rapidly to the volcanically-induced SAOD changes, it is not necessary to lag SW relative to SAOD; all $r\{\text{SAOD}, \text{SW}\}$ results in Fig. 3B and Supplementary Fig. 5B are for contemporaneous correlations.

9 Discussion of results

9.1 Regression coefficients

Because of collinearity between the ENSO predictor variable and volcanically-induced TLT variability, the regression coefficient b_j between X_t and T_t can differ markedly from the b_j value calculated after the first iteration[10]. Consider the example of observational TLT data spatially averaged over 20°N-20°S, with $\tau = 40$ months, $t_{\text{base}} = 6$

[10] After the first iteration, the regression coefficient is calculated using X_t and T_t^* (see section 8.1).

months, and $\Delta T_{\max}$ and t_{ramp} estimated from unsmoothed data. For RSS, $b_j = 0.695$ after the first iteration, 0.796 after the second iteration, and 0.798 after the 10th iteration (with the lag $j = 3$ months in each iteration). Ignoring collinearity yields an ENSO signal that explains less of the temporal variance of tropical TLT data.

9.2 Incomplete removal of volcano signals

The modelled and observed tropospheric temperature residuals after removal of ENSO and volcano signals, ε_t, are characterized by two small maxima. These maxima occur roughly 1-2 years after the peak cooling caused by El Chichón and Pinatubo (see Fig. 1C), and are probably related to incomplete removal of the El Chichón and Pinatubo cooling signals. Incomplete signal removal can occur for at least two reasons: 1) "contamination" of the Niño 3.4 SSTs used to estimate the ENSO TLT signal by volcanically-induced cooling (ref. 21); and 2) differences between the stipulated value of τ (40 months for the 28 models in Fig. 1C) and each model's actual value of τ.

Supplementary Fig. 3 shows that if each individual model's actual ECS value is used for calculating τ, the above-mentioned twin maxima in ε_t are not removed. This suggests that the first effect (volcanic "contamination" of X_t) is probably more important in explaining the residual maxima in ε_t.

9.3 Results from Vol21c simulations

After ENSO removal, the `GISS-E2-R` ensemble-mean TLT trend from 1998 to 2012 is 0.175°C/decade in the ALL+4.5 runs and 0.171°C/decade in the ALL+Vol21c simulations. The corresponding values are 0.327°C/decade and 0.287°C/decade for `CanESM`. Observed 'ENSO removed' TLT trends over the same time period are −0.016°C/decade and 0.071°C/decade for RSS and UAH. As noted in the main text, including more realistic volcanic aerosol forcing reduces the discrepancy between the model and observed TLT trends over the hiatus period. The reduction is larger for `CanESM` (11-15%) than for `GISS-E2-R` (2-4%).

References for Online Methods

31. Bourassa, A. E. *et al.* Large volcanic aerosol load in the stratosphere linked to Asian monsoon transport. *Science* **337**, 78-81 (2012).

32. Fröhlich, C. Observations of irradiance variations. *Space Sci. Rev.* **94**, 15-24 (2000).

33. Andrews, T., Gregory, J. M., Webb, M. J. & Taylor, K. E. Forcing, feedbacks and climate sensitivity in CMIP5 coupled atmosphere-ocean climate models. *Geophys. Res. Lett.* **39**, L09712, doi:10.1029/2012GL051607 (2012).

34. Gregory, J. M. *et al.* A new method for diagnosing radiative forcing and climate sensitivity. *Geophys. Res. Lett.* **31**, doi:10.1029/2003GL018747 (2004).

35. Santer, B. D. *et al.* Consistency of modelled and observed temperature trends in the tropical troposphere. *Int. J. Clim.* **28**, 1703-1722 (2008).

Supplementary Figure 1: Time series of simulated and observed monthly-mean near-global anomalies in the temperature of the lower stratosphere (TLS; panel A) and the lower troposphere (TLT; panel B). The stratospheric warming after the eruptions of El Chichón in 1982 and Pinatubo in 1991 occurs because volcanic aerosols absorb incoming solar and outgoing long-wave radiation; tropospheric cooling is caused by the aerosol-induced backscattering of solar radiation (ref. 17 and 19). Model results are from simulations with combined anthropogenic and natural external forcing (ALL+8.5). The bold lines denote the ALL+8.5 multi-model averages, calculated with the ensemble-mean temperature changes from 41 individual ALL+8.5 realizations (thin grey lines) performed with 28 CMIP-5 models. Observational results are from RSS (ref. 13) and UAH (ref. 14). Temperatures are averaged over the maximum common coverage between the RSS and UAH data sets (82.5°N-82.5°S for TLS, and 82.5°N-70°S for TLT). Anomalies are defined with respect to climatological monthly means over 1979 to 2012. Both models and observations show a large residual seasonal cycle in TLS, which is due to the pronounced seasonality in stratospheric ozone forcing (ref. 5).

Supplementary Figure 2: Removal of ENSO and volcano signals from observed lower tropospheric temperature data using an iterative regression-based method (refs. 20, 21). The example shown here relies on observed time series of monthly-mean changes in near-global TLT (panel A; ref. 13) and on SSTs averaged over the Niño 3.4 region (panel B; ref. 23). The estimate of the ENSO signal in TLT (panel C)

lags the Niño 3.4 SST time series by 5 months. Subtraction of the ENSO signal from the original TLT data reduces noise in the TLT response to the eruptions of El Chichón and Pinatubo (panel D). Values of the maximum volcanically-induced cooling ($\Delta T_{\rm max}$) and the "ramp time" to attain maximum cooling ($t_{\rm ramp}$) are estimated from the 'ENSO-removed' data, using four different stipulated values of the signal decay time τ. Volcanic signals are computed separately for El Chichón and Pinatubo (panel E). The El Chichón and Pinatubo signals are then removed from the original TLT data, and the ENSO signal is recalculated. Iteration continues until stable estimates of volcano and ENSO signals are obtained. The residuals after removal of El Chichón, Pinatubo, and ENSO signals are shown in panel F for $\tau = 40$ months. See Supplementary Methods for further details.

Supplementary Figure 3: Time series of observed (panels A, C) and simulated (panels B, D) monthly-mean, near-global anomalies in the temperature of the lower troposphere after statistical removal of ENSO effects and the signals of El Chichón and Pinatubo. After subtraction of ENSO signals, values of $\Delta T_{\rm max}$ and $t_{\rm ramp}$ were estimated from either unfiltered TLT data (panels A, B) or from TLT data smoothed with a five-term binomial filter to damp high-frequency noise (panels C, D). Volcanic signals were removed using four different stipulated values of the recovery time τ (30, 35, 40, and 45 months). In each of these four cases, results are multi-model averages, calculated with 41 realizations of the ALL+8.5 simulation, performed with 28 different models. We also consider a fifth case, in which volcanic signal subtraction

relies on τ values based on the equilibrium climate sensitivity (ECS) of individual CMIP-5 models. In the latter case, ECS estimates were available for 22 models only. Observations in panels A and C are from Remote Sensing Systems (ref. 13). All TLT results are for spatial averages over 82.5°N-70°S. Note that the discrepancy between modelled and observed TLT trends over 1998 to 2012 is relatively insensitive to uncertainties in τ.

Supplementary Figure 4: Time series of observed changes in tropical SAOD (panel A) and TLT (panel B) over January 1985 to December 2012. The SAOD results are updated versions of the data published by Vernier *et al.* (ref. 24) and Sato *et al.* (ref. 18). The altitude ranges are 15 to 40 km for the Vernier *et al.* SAOD measurements and 15 to 35 km (the maximum vertical extent) for version C of the Sato *et al.* SAOD data. The ENSO signal in TLT was removed with the iterative regression-based method (refs. 20, 21) described in the Supplementary Methods. A stipulated 40-month decay time was used for estimating the tropospheric temperature signals of El Chichón and Pinatubo. All SAOD and TLT data are spatial averages over 20°N-20°S, except for the Sato *et al.* SAOD data, which were averaged over 23.5°N-23.5°S. The start dates of larger eruptions are identified by colored vertical lines; solid (dashed) lines denote eruptions occurring within (outside) the 20°N-20°S latitude band.

Supplementary Figure 5: As for Fig. 3 of main text, but for SAOD, TLT, and net clear-sky SW radiation spatially averaged over 50°N-50°S (the latitudinal extent of the updated Vernier *et al.* SAOD data; see ref. 24).

Supplementary Figure 6: The impact of including improved estimates of the post-Pinatubo volcanic aerosol forcing on the "warming hiatus". The `GISS-E2-R (p3)` and `CanESM2` models were used to perform simulations with updated volcanic aerosol forcing ("Vol21c"; panels A and B, respectively). In both sets of Vol21c integrations, post-2005 changes in anthropogenic greenhouse gas and aerosol concentrations are prescribed according to the RCP4.5 scenario. To evaluate the impact of more realistic treatment of post-Pinatubo volcanic forcing, we compared the spliced ALL+Vol21c results with maximally-overlapping 10-year TLT trends from the spliced ALL+RCP4.5 simulations (see Supplementary Methods). Five realizations of the ALL+Vol21c and ALL+RCP4.5 simulations were available for each of the two models. The bold lines denote ensemble means. All model and observational results use $\tau = 40$ months for removing ENSO signals.

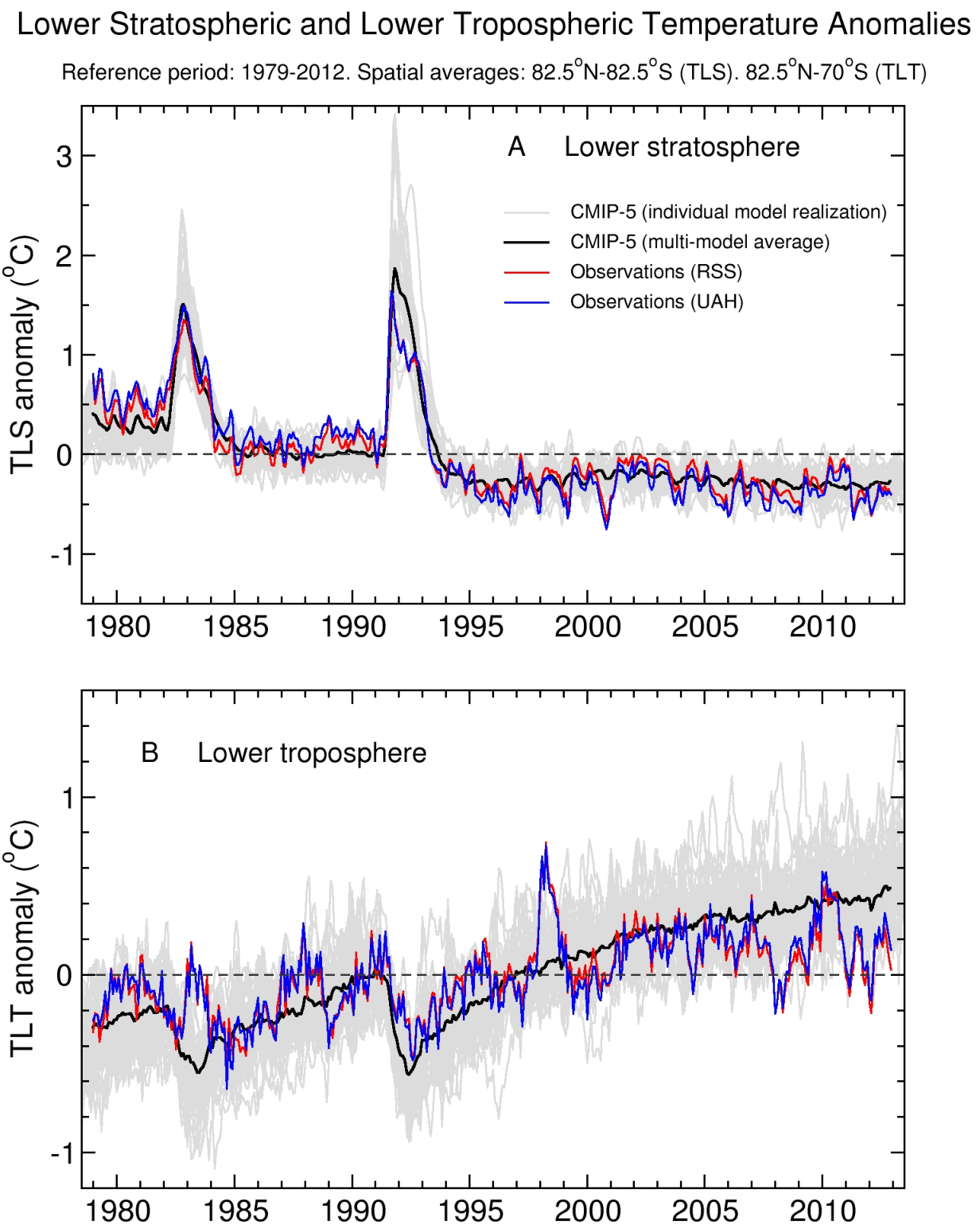

Extended Data Figure 1: Santer *et al.*

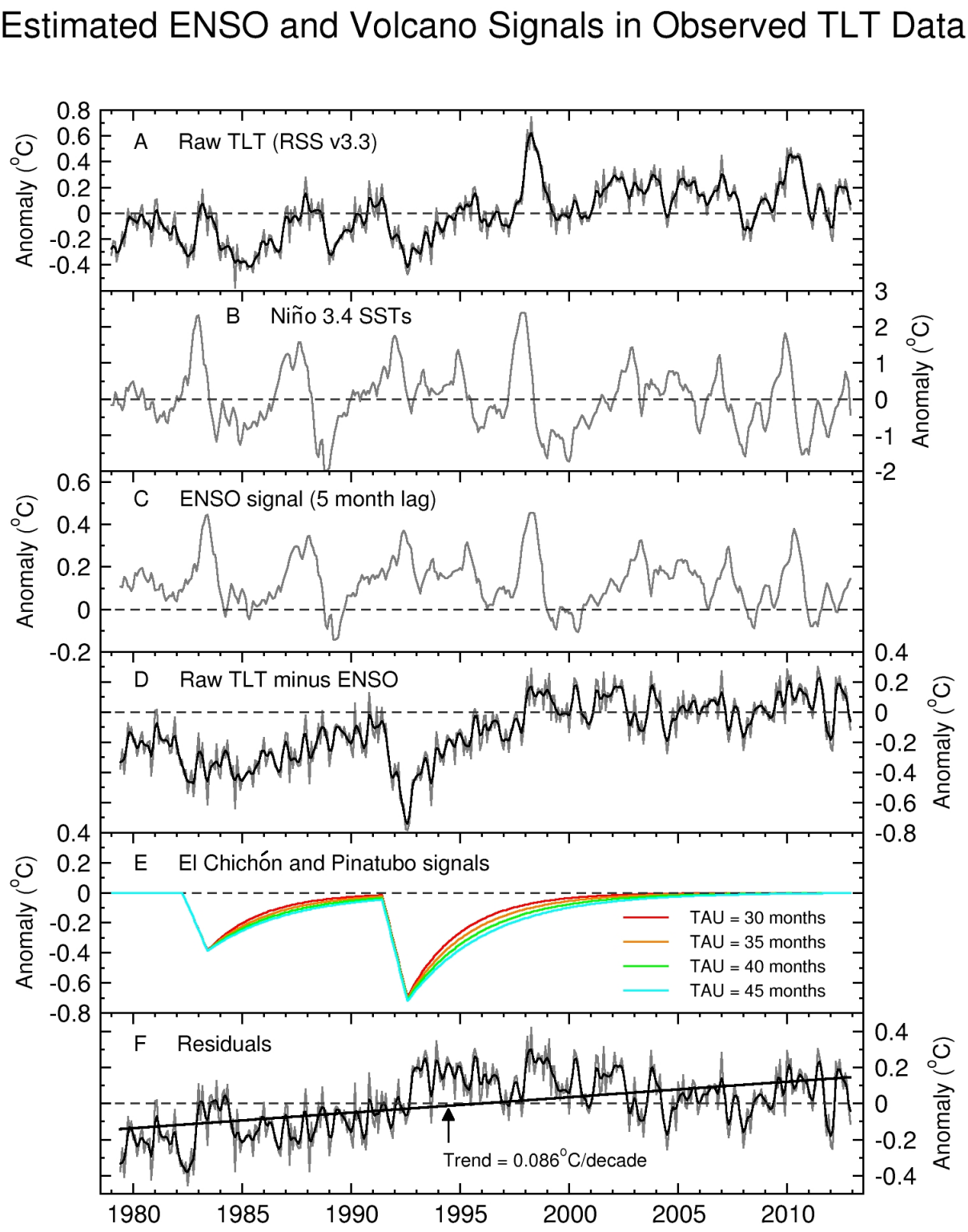

Extended Data Figure 2: Santer *et al.*

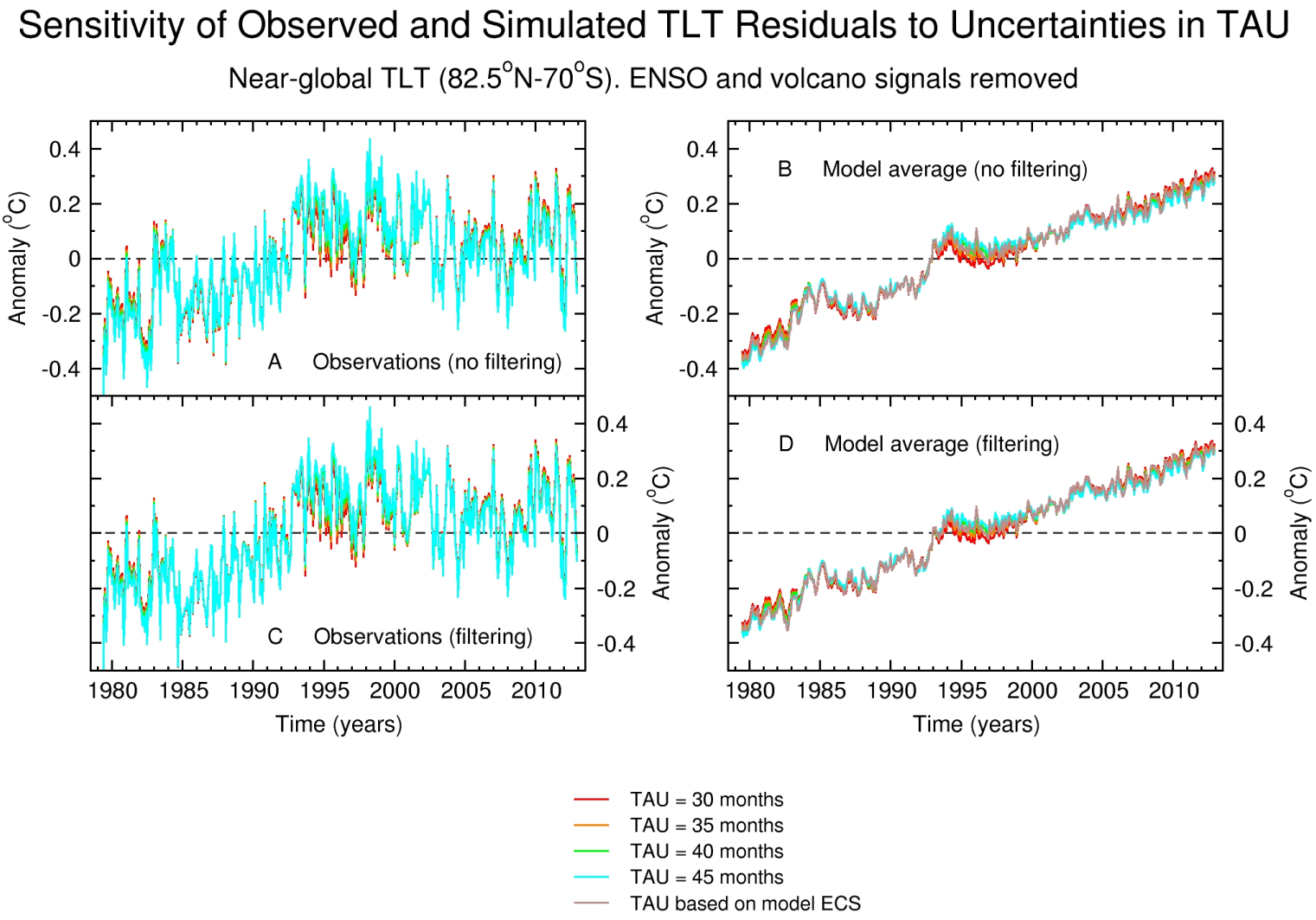

Extended Data Figure 3: Santer *et al.*

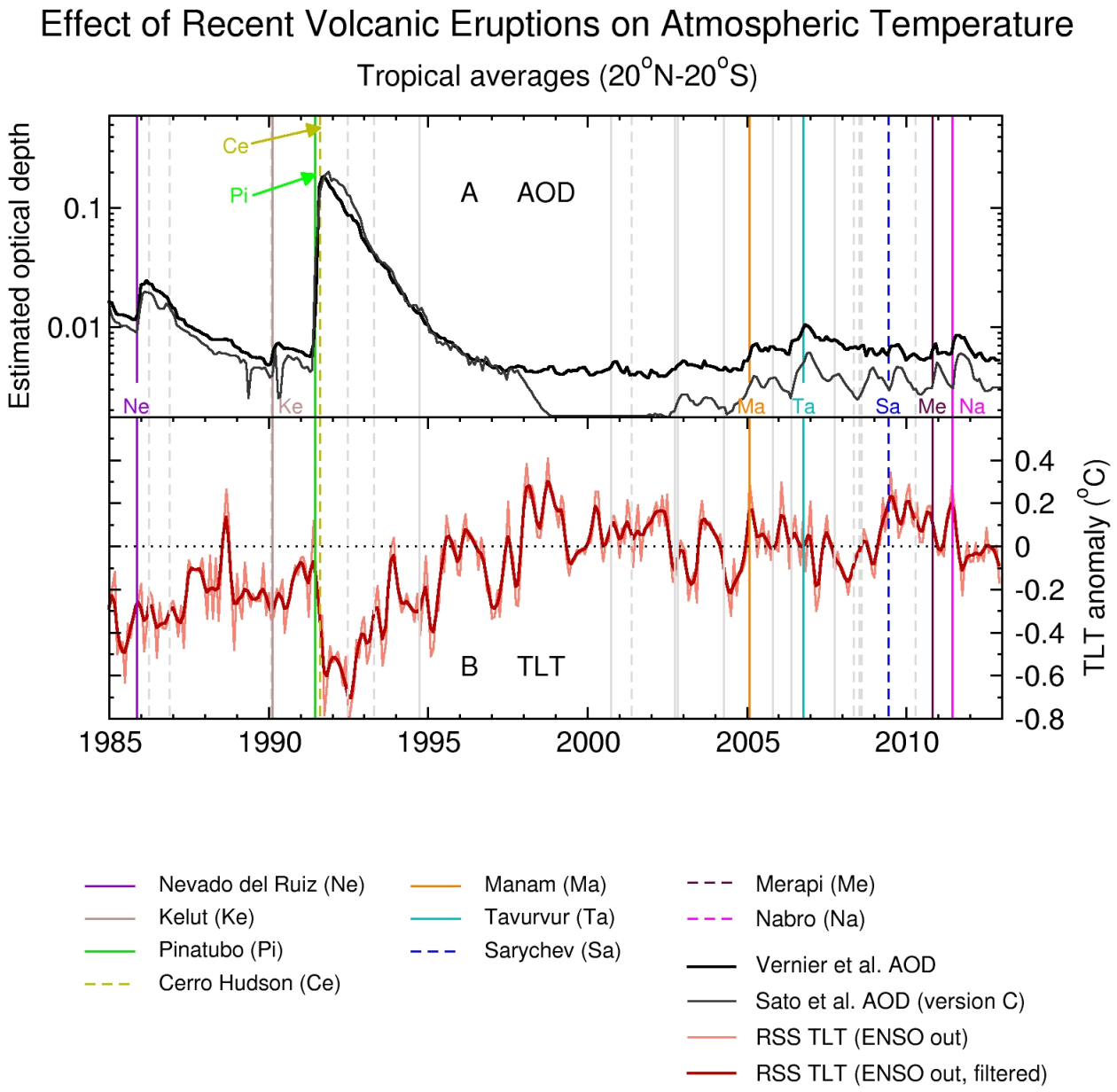

Extended Data Figure 4: Santer *et al.*

Significance of Observed Near-Global Climate Signals After Volcanic Eruptions

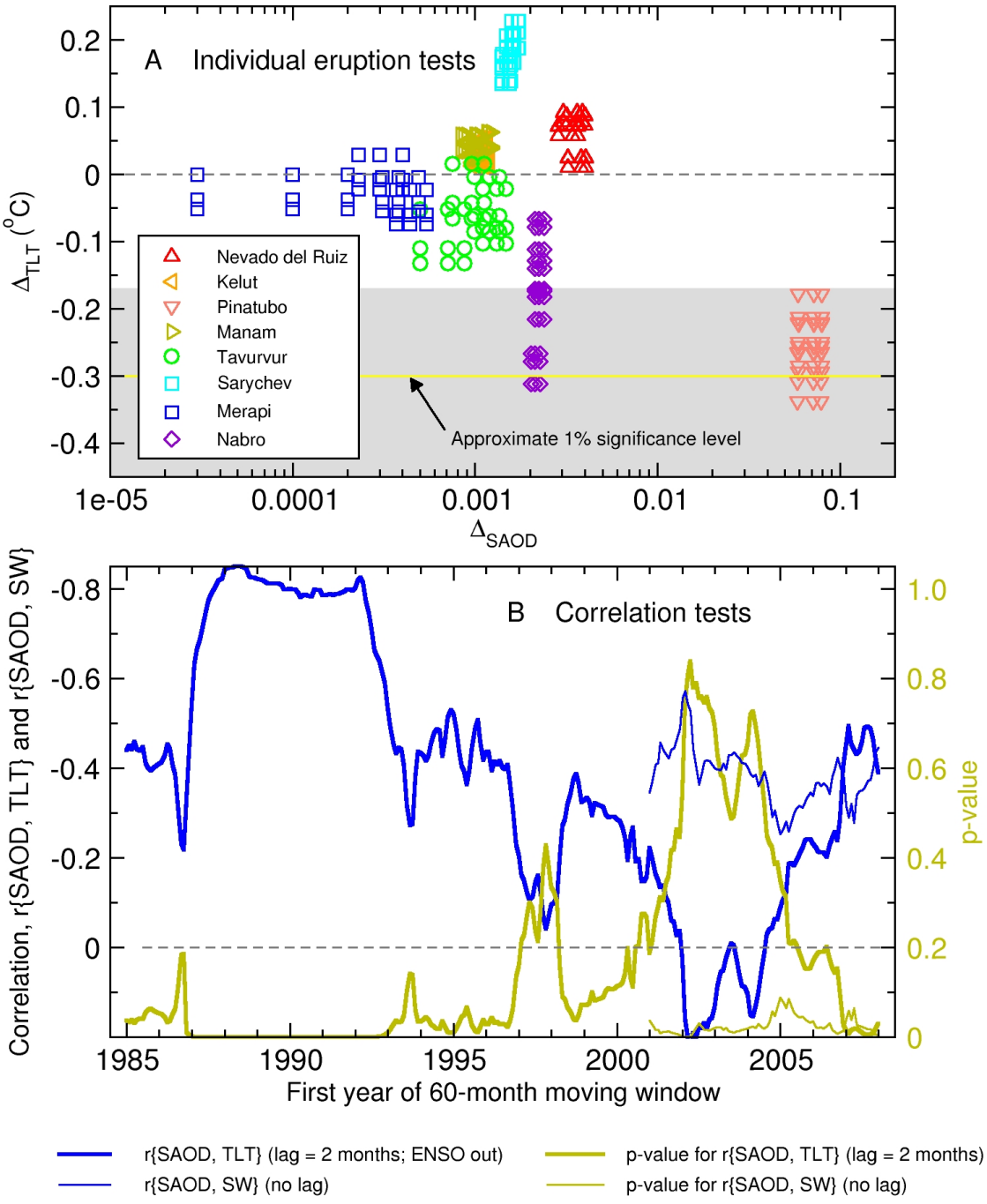

Extended Data Figure 5: Santer *et al.*

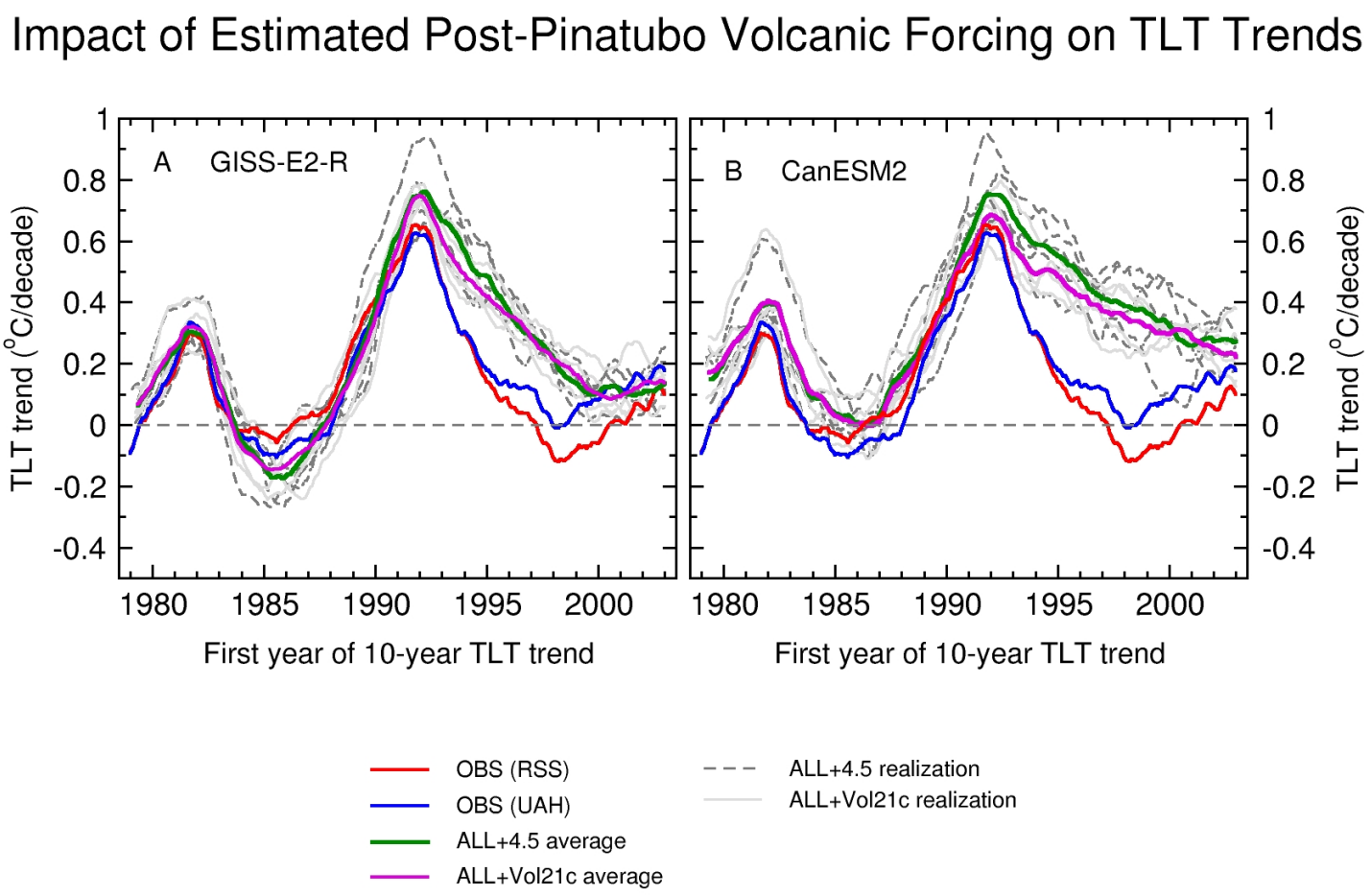

Extended Data Figure 6: Santer *et al.*

Supplementary Table 1: Modelling center information and official acronyms of the CMIP-5 models used in this study.

	Model	**Country**	**Modeling center**
1	ACCESS1.0	Australia	Commonwealth Scientific and Industrial Research Organization and Bureau of Meteorology
2	ACCESS1.3	Australia	Commonwealth Scientific and Industrial Research Organization and Bureau of Meteorology
3	BCC-CSM1.1	China	Beijing Climate Center, China Meteorological Administration
4	BCC-CSM1.1(m)	China	Beijing Climate Center, China Meteorological Administration
5	CanESM2	Canada	Canadian Centre for Climate Modelling and Analysis
6	CCSM4	USA	National Center for Atmospheric Research
7	CESM1(BGC)	USA	National Science Foundation, U.S. Dept. of Energy, National Center for Atmospheric Research
8	CESM1(CAM5)	USA	National Science Foundation, U.S. Dept. of Energy, National Center for Atmospheric Research
9	CNRM-CM5	France	Centre National de Recherches Meteorologiques / Centre Européen de Recherche et Formation Avancées en Calcul Scientifique
10	CSIRO-Mk3.6.0	Australia	Commonwealth Scientific and Industrial Research Organization in collaboration with Queensland Climate Change Centre of Excellence
11	EC-EARTH	Various	EC-EARTH consortium
12	GFDL-CM3	USA	NOAA Geophysical Fluid Dynamics Laboratory
13	GFDL-ESM2G	USA	NOAA Geophysical Fluid Dynamics Laboratory
14	GFDL-ESM2M	USA	NOAA Geophysical Fluid Dynamics Laboratory
15	GISS-E2-H (p1)	USA	NASA Goddard Institute for Space Studies

Supplementary Table 1: Modelling center information and official acronyms of the CMIP-5 models used in this study (continued).

	Model	**Country**	**Modeling center**
16	GISS-E2-R (p1)	USA	NASA Goddard Institute for Space Studies
17	GISS-E2-R (p2)	USA	NASA Goddard Institute for Space Studies
18	GISS-E2-R (p3)	USA	NASA Goddard Institute for Space Studies
19	HadGEM2-CC	UK	Met. Office Hadley Centre
20	HadGEM2-ES	UK	Met. Office Hadley Centre
21	MIROC5	Japan	Atmosphere and Ocean Research Institute (the University of Tokyo), National Institute for Environmental Studies, and Japan Agency for Marine-Earth Science and Technology
22	MIROC-ESM-CHEM	Japan	Japan Agency for Marine-Earth Science and Technology, Atmosphere and Ocean Research Institute (the University of Tokyo), and National Institute for Environmental Studies
23	MIROC-ESM	Japan	Japan Agency for Marine-Earth Science and Technology, Atmosphere and Ocean Research Institute (the University of Tokyo), and National Institute for Environmental Studies
24	MPI-ESM-LR	Germany	Max Planck Institute for Meteorology
25	MPI-ESM-MR	Germany	Max Planck Institute for Meteorology
26	MRI-CGCM3	Japan	Meteorological Research Institute
27	NorESM1-M	Norway	Norwegian Climate Centre
28	NorESM1-ME	Norway	Norwegian Climate Centre

Supplementary Table 2: External forcings in the historical simulations of the CMIP-5 models used in this study. Information was extracted from the global attribute named "forcing" in the metadata of the relevant NetCDF files[1].

	Model	Forcing information from metadata
1	ACCESS1.0	GHG, Oz, SA, Sl, Vl, BC, OC[2]
2	ACCESS1.3	GHG, Oz, SA, Sl, Vl, BC, OC[2]
3	BCC-CSM1.1	Nat, Ant, GHG, SD, Oz, Sl, Vl, SS, Ds, BC, OC
4	BCC-CSM1.1(m)	Nat, Ant, GHG, SD, Oz, Sl, Vl, SS, Ds, BC, OC
5	CanESM2	GHG, Oz, SA, BC, OC, LU, Sl, Vl
6	CCSM4	Sl, GHG, Vl, SS, Ds, SD, BC, MD, OC, Oz, AA, LU
7	CESM1-BGC	Sl, GHG, Vl, SS, Ds, SD, BC, MD, OC, Oz, AA, LU
8	CESM1-CAM5	Sl, GHG, Vl, SS, Ds, SD, BC, MD, OC, Oz, AA, LU
9	CNRM-CM5	GHG, SA, Sl, Vl, BC, OC[3]
10	CSIRO-Mk3.6.0	Ant, Nat
11	EC-EARTH	Nat, Ant
12	GFDL-CM3	GHG, SA, Oz, LU, Sl, Vl, SS, BC, MD, OC[4]
13	GFDL-ESM2G	GHG, SD, Oz, LU, Sl, Vl, SS, BC, MD, OC[5]
14	GFDL-ESM2M	GHG, SD, Oz, LU, Sl, Vl, SS, BC, MD, OC[5]
15	GISS-E2-H (p1)	GHG, LU, Sl, Vl, BC, OC, SA, Oz[6]
16	GISS-E2-R (p1)	GHG, LU, Sl, Vl, BC, OC, SA, Oz[6]
17	GISS-E2-R (p2)	GHG, LU, Sl, Vl, BC, OC, SA, Oz[6]
18	GISS-E2-R (p3)	GHG, LU, Sl, Vl, BC, OC, SA, Oz[6]
19	HadGEM2-CC	GHG, Oz, SA, LU, Sl, Vl, BC, OC
20	HadGEM2-ES	GHG, SA, Oz, LU, Sl, Vl, BC, OC[7]
21	MIROC5	GHG, SA, Oz, LU, Sl, Vl, SS, Ds, BC, MD, OC[8]

Supplementary Table 2 (continued): External forcings in the historical simulations of the CMIP-5 models used in this study.

Model	Forcing information from metadata
22 MIROC-ESM-CHEM	GHG, SA, Oz, LU, Sl, Vl, MD, BC, OC
23 MIROC-ESM	GHG, SA, Oz, LU, Sl, Vl, MD, BC, OC
24 MPI-ESM-LR	GHG, Oz, SD, Sl, Vl, LU
25 MPI-ESM-MR	GHG, Oz, SD, Sl, Vl, LU
26 MRI-CGCM3	GHG, SA, Oz, LU, Sl, Vl, BC, OC[9]
27 NorESM1-M	GHG, SA, Oz, Sl, Vl, BC, OC
28 NorESM1-ME	GHG, SA, Oz, Sl, Vl, BC, OC

[1]Forcing abbreviations are described in Appendix 1.2 of the CMIP-5 Data Reference Syntax document. Nat = natural forcing (a combination, not explicitly defined); Ant = anthropogenic forcing (a combination, not explicitly defined); GHG = well-mixed greenhouse gases; SD = anthropogenic sulfate aerosol (direct effects only); SI = anthropogenic sulfate aerosol (indirect effects only); SA = anthropogenic sulfate aerosol direct and indirect effects; Oz = tropospheric and stratospheric ozone; LU = land-use change; Sl = solar irradiance; Vl = volcanic aerosol; SS = sea salt; Ds = dust; BC = black carbon; MD = mineral dust; OC = organic carbon; AA = anthropogenic aerosols (a mixture of aerosols, not explicitly defined).

[2]GHG = CO_2, N_2O, CH_4, CFC11, CFC12, CFC113, HCFC22, HFC125, HFC134a.

[3]Although stratospheric ozone forcing is not listed in the forcing metadata, chlorine concentration is an input for the prognostic ozone scheme of the `CNRM-CM5` model. So according to the CMIP-5 Data Reference Syntax document, stratospheric ozone should have been listed as an external forcing.

[4]GHG includes CO_2, CH_4, N_2O, CFC11, CFC12, HCFC22, and CFC113. Aerosol direct and indirect effects are included.

[5]GHG includes CO_2, CH_4, N_2O, CFC11, CFC12, HCFC22, and CFC113. "The direct effect of tropospheric aerosols is calculated by the model, but not the indirect effects."

[6]Also includes orbital change, BC on snow, and nitrate aerosols.

[7]GHG = CO_2, N_2O, CH_4, CFCs.

[8]GHG includes CO_2, N_2O, CH_4, and CFCs; Oz includes OH and H_2O_2; LU excludes change in lake fraction.

[9]GHG includes CO_2, CH_4, N_2O, CFC-11, CFC-12, and HCFC-22.

Supplementary Table 3: Start dates, end dates, and lengths (N_m, in months) of the CMIP-5 historical and RCP8.5 simulations used in this study. EM is the "ensemble member" identifier described in the CMIP-5 Data Reference Syntax document[1].

	Model	EM	Hist. Start	Hist. End	Hist. N_m	RCP8.5 Start	RCP8.5 End	RCP8.5 N_m
1	ACCESS1.0	r1i1p1	1850-01	2005-12	1872	2006-01	2100-12	1140
2	ACCESS1.3	r1i1p1	1850-01	2005-12	1872	2006-01	2100-12	1140
3	BCC-CSM1.1	r1i1p1	1850-01	2012-12	1956	2006-01	2300-12	3540
4	BCC-CSM1.1(m)	r1i1p1	1850-01	2012-12	1956	2006-01	2099-12	1128
5	CanESM2	r1i1p1	1850-01	2005-12	1872	2006-01	2100-12	1140
6	CanESM2	r2i1p1	1850-01	2005-12	1872	2006-01	2100-12	1140
7	CanESM2	r3i1p1	1850-01	2005-12	1872	2006-01	2100-12	1140
8	CanESM2	r4i1p1	1850-01	2005-12	1872	2006-01	2100-12	1140
9	CanESM2	r5i1p1	1850-01	2005-12	1872	2006-01	2100-12	1140
10	CCSM4	r1i1p1	1850-01	2005-12	1872	2006-01	2100-12	1140
11	CCSM4	r2i1p1	1850-01	2005-12	1872	2006-01	2100-12	1140
12	CCSM4	r3i1p1	1850-01	2005-12	1872	2006-01	2100-12	1140
13	CESM1-BGC	r1i1p1	1850-01	2005-12	1872	2006-01	2100-12	1140
14	CESM1-CAM5	r1i1p1	1850-01	2005-12	1872	2006-01	2100-12	1140
15	CNRM-CM5	r1i1p1	1850-01	2005-12	1872	2006-01	2300-12	3540
16	CNRM-CM5	r2i1p1	1850-01	2005-12	1872	2006-01	2100-12	1140
17	CNRM-CM5	r4i1p1	1850-01	2005-12	1872	2006-01	2100-12	1140
18	CSIRO-Mk3.6.0	r10i1p1	1850-01	2005-12	1872	2006-01	2100-12	1140
19	EC-EARTH	r8i1p1	1850-01	2012-12	1956	2006-01	2100-12	1140
20	GFDL-CM3	r1i1p1	1860-01	2005-12	1752	2006-01	2100-12	1140
21	GFDL-ESM2G	r1i1p1	1861-01	2005-12	1740	2006-01	2100-12	1140
22	GFDL-ESM2M	r1i1p1	1861-01	2005-12	1740	2006-01	2100-12	1140

Supplementary Table 3 (continued): Start dates, end dates, and lengths of the CMIP-5 historical and RCP8.5 simulations used in this study.

	Model	EM	Hist. Start	Hist. End	Hist. (months)	RCP8.5 Start	RCP8.5 End	RCP8.5 (months)
23	GISS-E2-H (p1)	r1i1p1	1850-01	2005-12	1872	2006-01	2300-12	3540
24	GISS-E2-R (p1)	r1i1p1	1850-01	2005-12	1872	2006-01	2300-12	3540
25	GISS-E2-R (p2)	r1i1p2	1850-01	2005-12	1872	2006-01	2300-12	3540
26	GISS-E2-R (p3)	r1i1p3	1850-01	2005-12	1872	2006-01	2300-12	3540
27	HadGEM2-CC	r1i1p1	1859-12	2005-11	1752	2005-12	2099-12	1129
28	HadGEM2-CC	r2i1p1	1959-12	2005-12	553	2005-12	2099-12	1129
29	HadGEM2-CC	r3i1p1	1959-12	2005-12	553	2005-12	2099-12	1129
30	HadGEM2-ES	r1i1p1	1859-12	2005-11	1752	2005-12	2299-12	3529
31	HadGEM2-ES	r2i1p1	1859-12	2005-12	1753	2005-12	2100-11	1140
32	MIROC5	r1i1p1	1850-01	2012-12	1956	2006-01	2100-12	1140
33	MIROC-ESM-CHEM	r1i1p1	1850-01	2005-12	1872	2006-01	2100-12	1140
34	MIROC-ESM	r1i1p1	1850-01	2005-12	1872	2006-01	2100-12	1140
35	MPI-ESM-LR	r1i1p1	1850-01	2005-12	1872	2006-01	2300-12	3540
36	MPI-ESM-LR	r2i1p1	1850-01	2005-12	1872	2006-01	2100-12	1140
37	MPI-ESM-LR	r3i1p1	1850-01	2005-12	1872	2006-01	2100-12	1140
38	MPI-ESM-MR	r1i1p1	1850-01	2005-12	1872	2006-01	2100-12	1140
39	MRI-CGCM3	r1i1p1	1850-01	2005-12	1872	2006-01	2100-12	1140
40	NorESM1-M	r1i1p1	1850-01	2005-12	1872	2006-01	2100-12	1140
41	NorESM1-ME	r1i1p1	1850-01	2005-12	1872	2006-01	2100-12	1140

[1]See http://cmip-pcmdi.llnl.gov/cmip5/documents.html for further details.

Supplementary Table 4: Information relating to the timing, location, and explosivity of 21st century volcanic eruptions with a Volcanic Explosivity Index (VEI) ≥ 3. Note that DY ("Decimal Year") is the eruption date expressed in decimal form.

	Volcano	Abb.	Source[1]	Date[2]	DY[3]	Lat.	Lon.	VEI
1	Ulawun	Ul	N, V	Sept. 29, 2000	2000.74	5.1°S	151.3°E	4
2	Shiveluch	Sh	V	May 22, 2001	2001.39	56.7°N	161.4°E	4?
3	Ruang	Ru	N, V	Sept. 25, 2002	2002.73	2.3°N	125.4°E	4?
4	Reventador	Ra	N, V	Nov. 3, 2002	2002.83	0.1°S	77.7°W	4
5	Anatahan	At	N	Apr. 12, 2004	2004.28	16.4°N	145.7°E	3?
6	Manam	Ma	N, V	Jan. 27, 2005	2005.07	4.1°S	145.0°E	4
7	Sierra Negra	Si	N	Oct. 22, 2005	2005.81	0.8°S	91.2°W	3
8	Soufrière Hills	So	N, V	May 20, 2006	2006.38	16.7°N	62.2°W	4?
9	Tavurvur	Ta	N, V	Oct. 7, 2006	2006.76	4.3°S	152.2°E	4?
10	Jebel at Tair	Jb	N	Sep. 30, 2007	2007.75	15.6°N	41.8°E	3?
11	Chaitén	Ch	N, V	May 2, 2008	2008.34	42.8°S	72.6°W	4
12	Okmok	Ok	N, V	Jul. 12, 2008	2008.53	53.4°N	168.1°W	4
13	Kasatochi	Ka	N, V	Aug. 7, 2008	2008.60	52.2°N	175.5°W	4
14	Sarychev	Sa	N, V	Jun. 12, 2009	2009.44	48.1°N	153.2°E	4?
15	Eyjafjallajökull	Ey	U	Apr. 14, 2010	2010.28	63.6°N	19.6°W	4
16	Merapi	Me	U	Oct. 26, 2010	2010.82	7.5°S	110.4°E	4
17	Nabro	Na	B	Jun. 13, 2011	2011.45	13.4°N	41.7°E	?

[1]Sources of information are: Neely *et al.*, 2013 (N) (ref. 25); Vernier *et al.*, 2011 (V) (ref. 24); Bourassa *et al.*, 2012 (B) (ref. 31), and U.S. Geological Survey (U). Information from the latter source was available at http://www.volcano.si.edu/reports/usgs/.

[2]For some volcanic events (such as Shiveluch in 2001 and Eyjafjallajökull in 2010), there is ambiguity in estimating the exact eruption date.

[3]The "decimal year" (ref. 25) is the total number of days from the beginning of the year to the eruption date, divided by 365 (366 for leap years).